Received: Added at production | Revised: Added at production | Accepted: Added at production

DOI: xxx/xxxx

ARTICLE TYPE

A discontinuous Nitsche-based Finite Element formulation for the imposition of the Navier-slip condition over embedded volumeless geometries

R. Zorrilla*[1] | A. Larese[2] | R. Rossi[1,3]

[1]International Center for Numerical Methods in Engineering (CIMNE), Kratos Multiphysics Group, Barcelona, Spain
[2]Università degli Studi di Padova, Department of Mathematics "Tullio Levi-Civita", Padova, Italy
[3]Universitat Politècnica de Catalunya (UPC), Department of Civil and Environmental Engineering (DECA), Barcelona, Spain

Correspondence
*R. Zorrilla, CIMNE - Edifici C1 Campus Nord UPC C/ Gran Capità, S/N 08034 Barcelona, Spain. Email: rzorrilla@cimne.upc.edu

Summary

This work describes a novel formulation for the simulation of incompressible Navier-Stokes problems involving nonconforming discretizations of membrane-like bodies. The new proposal relies on the use of a modified finite element space within the elements intersected by the embedded geometry, which is represented by a discontinuous (or element-by-element) level set function. This is combined with a Nitsche-based imposition of the general Navier-slip boundary condition, to be intended as a wall law model. Thanks to the use of an alternative finite element space, the formulation is capable of reproducing exactly discontinuities across the embedded interface, while preserving the structure of the graph of the discrete matrix. The performance, accuracy and convergence of the new proposal is compared with analytical solutions as well as with a body fitted reference technique. Moreover, the proposal is tested against another similar embedded approach. Finally, a realistic application showcasing the possibilities of the method is also presented.

KEYWORDS:
Embedded Boundary Methods, Navier-Stokes, Membrane, Nitsche method, Navier-slip

1 | INTRODUCTION

During the last decades, Computational Fluid Dynamics (CFD) has become an essential tool in multiple engineering disciplines. These range from civil engineering, for example for the simulation of structures under the action of severe or dynamic wind loads [1], to biomedical where CFD is used for the investigation of cardiovascular diseases [2,3]. In this work, we target the simulation of general incompressible viscous flows as the ones that can be found in these, or similar, applications. Although this objective can be achieved by using alternative approaches, such as the Finite Volume Method (FVM) [4,5] or the Particle Finite Element Method (PFEM) [6], we focus on fixed grid (Eulerian) Finite Element Method (FEM) [7].

Grid-based discretization methods can be broadly divided into two main families: body conforming (also known as body-fitted) discretizations and nonconforming (or unfitted) discretizations. In the body fitted case, the boundaries of the volume (fluid) mesh match, as closely as possible, the shape of the object(s) of interest. On the contrary, in the nonconforming case the discretization of the fluid volume and that one of the analysed object are constructed independently. This is typically achieved by superimposing the latter to the background mesh in order to perform an automatic intersection operation. Hence, the shape of the object can be represented onto the background mesh as the zero isosurface of a signed distance function, which is computed from the immersed body skin intersections. This approach is well known as the level set method [8].

In general terms, nonconforming mesh discretizations feature a more intricate implementation and show limited accuracy when compared to their body fitted counterparts. However, they enjoy crucial advantages in dealing with large boundary movements that make Arbitrary Lagrangian-Eulerian (ALE) approaches [7,9] to fail due to mesh entangling. This enhanced capability has been successfully exploited for example in [10] for the simulation of a rotating mixer, in [11] to study the flapping of insect wings as well as the hydrodynamics of fish fins, in [12] to study the motion jellyfishes or in [13] to study the human cell motion.

Moreover, the use of a level set-type approach also provides a major advantage in dealing with "dirty" input geometries (i.e. surface geometries with undesired holes and overlapping entities with potential inconsistent orientation of the surface normals). This is due to the fact that finding the distance to an object is a geometrically robust operation that makes possible to automatically filter out the unresolved details of the degenerated input geometry [14].

Unfortunately, the enhanced robustness of the level set method comes at the price of a boundary representation accuracy that is worse than the one of standard body conforming techniques. Considering that it is impossible to get rid of this limitation, as it is inherent to the level set method, one can establish an alternative framework to deal with it. Hence, starting from a fast initial discretization, which can be for instance obtained by using an octree approach as in [15], one could adaptively refine it as needed by using robust methods based on local improvements [16,17,18]. This same workflow is also valid for the simulation of thin-walled bodies (i.e. shell and membrane structures) which can be effectively described in terms of embedded conditions for the pressure and velocity fields.

Over the years, the advantages of unfitted mesh discretizations led to the development of a wide variety of approaches such as the Immersed Boundary Method (IBM) [19,20], the eXtended Finite Element Method (X-FEM) [21,22,23,24], the Fictitious Domain Method (FDM) [25,26,27,28], the Embedded Boundary Method (EBM) [29], also known as Cut Finite Element Method (Cut-FEM), and, more recently, the Shifted Boundary Method (SBM) [30,31]. Besides these, the so called Immersogeometric approaches [32,33] also deserve a mention owing to their capability to combine exact geometries with nonconforming formulations.

All these methods share the need of imposing the Boundary Conditions (BCs) in an unfitted manner. This problem, which is an issue on its own, is customary solved by enforcing the BCs in a weak sense using techniques such as the penalty method [34], the Lagrange multipliers method [35,36] or the Nitsche method [37,38,39,40,26].

Among these techniques, in this work we favour the use of the Nitsche method. On the one hand, the Nitsche method is reported to have enhanced stability when compared with penalty-based impositions. On the other hand, as a difference from Lagrange multiplier approaches, it does not introduce extra degrees of freedom. This implies thus that the discrete sparse matrix graph does not need to be recomputed each time the level set function is updated, something that becomes crucial for the efficient extension of the method to Fluid-Structure Interaction (FSI) problems.

While in [28] [41] and [42] the authors apply different flavours of the Nitsche method to impose the no-slip condition, in [43] it is used to enforce a slip condition in Stokes flows. In [44] this is extended to the application of a general Navier-slip condition to the viscous incompressible Navier-Stokes equations. All these Nitsche-based approaches rely on the proper definition of an internal volume, something that requires distinguishing between the "inside" and "outside" regions of the objects of interest. Unfortunately, the inside/outside concept becomes meaningless as soon as thin-walled bodies are considered This therefore impedes the application of all the previous techniques to the analysis of volumeless geometries (e.g. shell or membrane structures).

Although this limitation can be overcome in an IBM fashion by adding an artificial volume force representing the immersed volumeless body [45,19,46] or by using ghost cell methods [11], we prefer to stick to Cut-FEM type approaches as these allow to obtain accurate solutions using a purely local BC imposition. In [47] the common Finite Element (FE) space is substituted by a discontinuous one [48] [1] in those elements intersected by the level set. Thanks to such FE space substitution, the velocity and pressure fields in both sides of an intersected element become disconnected, allowing thus the representation of the solution discontinuities arising from the thin-walled body immersion. This method is completed with a penalty-based imposition of a pure slip BC.

One of the objectives of this work is to enhance the capabilities of the method proposed in [47] by combining the Ausas space with a wall law, something that to the best of our knowledge has never been considered. Hence, we propose blending the Nitsche-based Navier-slip method in [44] with the discontinuous formulation in [47]. It is important to mention that the possibility of considering a wall law on the embedded boundaries becomes crucial in those scenarios featuring a poor boundary layer mesh resolution. Even though adaptive mesh refinement can be used to tackle such limitation, it rapidly becomes unaffordable when the bodies move across the background mesh (i.e. FSI) since adaptive refinement is likely required at each time step.

[1] From now on we will denote this modified discontinuous FE space as Ausas FE space after the name of the main original author

We note that the particular nature of the Ausas space, which implies a constant interpolation with zero gradient within one half of the intersected elements, is quite different to that one of classical Cut-FEM approaches. Thus, this requires the assessment of the Nitsche-based imposition behavior since correctness cannot be directly assumed from similar Cut-FEM approaches results. Furthermore, we clearly state that the current work intentionally avoids discussing the FSI case, as this would imply taking into account many practical aspects inherent to the embedded formulation and the coupling[49]. Instead, we focus on the proposed discontinuous Navier-slip formulation details as well as on its validation, which we carry out by comparing its performance with the approaches in[44] and[47]. We refer the reader to[50] for the extension of current formulation to FSI problems.

A further aspect that needs to be taken into account when dealing with embedded formulations is that "isolated" fluid domain cavities ("bubbles") can easily manifest within the domain, specially when degenerated input geometries are involved. For example, if we consider the 2D flow around a thin-walled cylinder, the fluid within the cylinder is isolated from the boundary, which in turn means that it is not subjected to any Neumann condition. The practical implication of this is that the discrete problem becomes unsolvable as the pressure is defined up to a constant for the portion of fluid inside the cylinder. Different options exist to handle this problem. One option is to identify the isolated cavities by looping the FEM discrete graph in order to apply the minimal pressure condition. While doable, this option requires implementing a graph search, which is expensive, particularly in the context of distributed solution procedures. Instead, our choice is to add an extra compressibility term to the formulation This ensures that the pressure constant is defined by the initial condition. The effectiveness of this approach is shown in the third example of this work.

Finally we shall mention that the formulation discussed in this work has been implemented in the Kratos Multiphysics open source framework[51,52].

2 | FORMULATION

This section presents the Navier-Stokes formulation we solve. Firstly, we present the pseudo-compressible viscous Navier-Stokes governing equations. Secondly, the stabilization technique we employ is briefly described. Finally, the Galerkin functional to be implemented is also presented.

2.1 | Governing equations

In this work we focus on the solution of the viscous Navier-Stokes equations. A Newtonian behaviour of the type $\boldsymbol{\sigma} = -p\mathbf{I} + \mathbb{C} : \boldsymbol{\nabla}^s\mathbf{u}$, being $\mathbf{u}$ the velocity, p the pressure, $\boldsymbol{\nabla}^s$ the symmetric gradient operator and $\mathbb{C}$ the shear stress Newtonian constitutive tensor. Upon substitution in the momentum and mass balance equations, we obtain the viscous incompressible Navier-Stokes equations

$$\rho\frac{\partial\mathbf{u}}{\partial t} + \rho\mathbf{u}\cdot\boldsymbol{\nabla}\mathbf{u} - \boldsymbol{\nabla}\cdot(\mathbb{C} : \boldsymbol{\nabla}^s\mathbf{u}) + \boldsymbol{\nabla}p = \rho\mathbf{b} \tag{1a}$$

$$\frac{D\rho}{Dt} + \rho\boldsymbol{\nabla}\cdot\mathbf{u} = 0 \tag{1b}$$

in which ρ represents the density and $\mathbf{b}$ the volume (body) forces. The operator $\partial(\bullet)/\partial t$ denotes the partial time derivative, $D(\bullet)/Dt$ the total time derivative and $\boldsymbol{\nabla}$ the gradient operator.

Moreover, we take the simplified sound speed (c) equation $p = \rho c^2 \;\Rightarrow\; c^2 = \partial p/\partial\rho$ as equation of state. This assumption, which is valid for almost incompressible fluids, allows us to rewrite the density time derivative in terms of the pressure. If we further assume that $\boldsymbol{\nabla}\rho \approx \mathbf{0}$, physically expressing that density fluctuations are negligible, the final form of the governing equations is

$$\rho\frac{\partial\mathbf{u}}{\partial t} + \rho\mathbf{u}\cdot\boldsymbol{\nabla}\mathbf{u} - \boldsymbol{\nabla}\cdot(\mathbb{C} : \boldsymbol{\nabla}^s\mathbf{u}) + \boldsymbol{\nabla}p = \rho\mathbf{b} \tag{2a}$$

$$\frac{1}{\rho c^2}\frac{\partial p}{\partial t} + \boldsymbol{\nabla}\cdot\mathbf{u} = 0 \tag{2b}$$

We note that the inclusion of a compressibility term in the mass conservation equation is not needed (and can be effectively omitted by setting a large speed of sound value) as long as a Neumann BC is applied in any part of the boundary. Nonetheless, the compressible term becomes very useful when isolated fluid cavities without any Neumann BC are found within the solution domain. In this context, the inclusion of such pseudo-compressibility effectively fixes the undetermined pressure constant, thus

making possible the resolution of the problem. This capapbility is proved in the pressurized cylinder example, which verifies that the speed of sound extra term allows the resolution of an otherwise unsolvable problem.

For a more detailed description of the derivation and implementation of the weakly compressible Navier-Stokes equations the reader is referred to [47].

2.2 | Stabilization

In this work we only consider simplicial elements with same velocity and pressure interpolation order. This type of elements do not satisfy the *inf-sup condition* and therefore require the use of a stabilization method [53]. Among all the stability approaches that have been reported to be valid for similar problems, we highlight the Galerkin Least Squares (GLS) [54], the Finite Increment Calculus (FIC) [55] and the Variational Multiscales Method (VMS) [56,57], which is the one adopted in this work. The VMS idea roots on the separation of the velocity $\mathbf{u}$ and pressure p fields in a FE resolvable scale and an unresolvable one as

$$\mathbf{u} = \mathbf{u_h} + \mathbf{u_s} \tag{3a}$$

$$p = p_h + p_s \tag{3b}$$

where the subscript h denotes the FE resolvable scales and the s one the fluctuations (subscales) that cannot be captured by the FE mesh and need thus to be modeled. A model for the subscales can be obtained by assuming these to be proportional to a projection of the FE residual onto the subscale space. The choice of an orthogonal projection operator leads to the Orthogonal Sub-Grid Scales (OSS) method [58]. In this work we take the identity as projection operator, leading to the so called Algebraic Sub-Grid Scales (ASGS) formulation [59]. Therefore, the velocity and pressure subscales are modelled as

$$\mathbf{u_s} = \tau_1 \mathbf{R^M}(\mathbf{u_h}, p_h) \tag{4a}$$

$$p_s = \tau_2 R^C(\mathbf{u_h}, p_h) \tag{4b}$$

where τ_1 and τ_2 are the so called stabilization constants and $\mathbf{R^M}$ and R^C the FE residuals of the momentum and mass conservation equations, which are defined as

$$\mathbf{R^M}(\mathbf{u_h}, p_h) = \rho\mathbf{b} - \rho\frac{\partial \mathbf{u_h}}{\partial t} - \rho\mathbf{u_h}\cdot\boldsymbol{\nabla}\mathbf{u_h} + \boldsymbol{\nabla}\cdot\left(\mathbb{C} : \boldsymbol{\nabla}^s\mathbf{u_h}\right) - \boldsymbol{\nabla}p_h \tag{5a}$$

$$R^C(\mathbf{u_h}, p_h) = -\frac{1}{\rho c^2}\frac{\partial p_h}{\partial t} - \boldsymbol{\nabla}\cdot\mathbf{u_h} \tag{5b}$$

The stabilization constants are taken from [59] and can be computed as

$$\tau_1 = \left(\frac{\rho\tau_{dyn}}{\Delta t} + \frac{c_2\rho\|\mathbf{u_h}\|}{h} + \frac{c_1\mu}{h^2}\right)^{-1} \tag{6a}$$

$$\tau_2 = \frac{h^2}{c_1\tau_1} \tag{6b}$$

being τ_{dyn} a parameter bounded between 0 and 1, $c_1 = 4.0$, $c_2 = 2.0$, $\|\mathbf{u}\|$ the L^2-norm of the convective velocity, μ the dynamic viscosity and h the element size, which we compute as the average of the heights associated to each element node.

We shall note that the subscales are, in fact, time dependent (Eq. 5). As it is discussed in [60], considering such time dependency enhances the formulation. However, such improvement comes at the price of increasing the complexity and computational effort of the formulation as it introduces the need of storing the subscales historical data in every integration point. Taking this into consideration, we decide to neglect the time dependency of the subscales by assuming that $\partial\mathbf{u_s}/\partial t \approx \mathbf{0}$ and $\partial p_s/\partial t \approx 0$, leading thus to a *quasi-static subscales formulation*.

2.3 | Variational form

After introducing the standard notation $(\bullet,\bullet)_\Omega$ to denote the inner product volume integrals and $\langle\bullet,\bullet\rangle_\Gamma$ for the boundary ones, the Galerkin functional to be solved can be defined as

$$\Psi(\mathbf{w}, q, \mathbf{u}, p) := \left(\mathbf{w}, \mathbf{R^M}(\mathbf{u}, p)\right)_\Omega + \left(q, R^C(\mathbf{u}, p)\right)_\Omega \tag{7}$$

where $\mathbf{w}$ and q are the velocity and pressure test functions.

Hence, after applying the scales decomposition in Eq. 3 to the defintion of the momentum and mass conservation residuals in Eq. 5 as well as integration by parts, the Galerkin functional above results in

$$\begin{aligned}&(\mathbf{w}, \rho\mathbf{b})_\Omega - \left(\mathbf{w}, \rho\frac{\partial \mathbf{u_h}}{\partial t}\right)_\Omega - \left(\mathbf{w}, \rho\mathbf{u_h}\cdot\nabla\mathbf{u_h}\right)_\Omega - \left(\nabla^s\mathbf{w}, \mathbb{C} : \nabla^s\mathbf{u_h}\right)_\Omega + \\ &\left(\nabla\cdot\mathbf{w}, p_h\right)_\Omega - \left(q, \frac{1}{\rho c^2}\frac{\partial p_h}{\partial t}\right)_\Omega - \left(q, \nabla\cdot\mathbf{u_h}\right)_\Omega + \langle\mathbf{w}, \mathbf{t}\rangle_\Gamma + \\ &\left(\rho\mathbf{u_h}\nabla\mathbf{w}, \mathbf{u_s}\right)_\Omega + \left(\rho(\nabla\cdot\mathbf{u_h})\mathbf{w}, \mathbf{u_s}\right)_\Omega + \left(\nabla\cdot\mathbf{w}, p_s\right)_\Omega + \left(\nabla q, \mathbf{u_s}\right)_\Omega = 0\end{aligned} \tag{8}$$

where $\mathbf{t}$ denotes the Cauchy traction vector, computed as $\mathbf{t} = \left(\mathbb{C} : \nabla^s\mathbf{u_h} - p_h\mathbf{I}\right)\cdot\mathbf{n}$, being $\mathbf{n}$ the boundary outwards unit vector.

The discrete functional in Eq. 8 can be implemented using a Computer Algebra System (CAS) to automatically obtain the elemental Left Hand Side (**LHS**) and Right Hand Side (**RHS**) matrices. Among the many libraries that support such capability, we selected the Python SymPy module[61]. A more comprehensive derivation of the variational form of the problem can be found in[47]. The automatic differentiation implementation is also available in the Kratos Multiphysics repository.

3 | NAVIER-SLIP EMBEDDED BOUNDARY CONDITION

This section presents the EBM that we propose for the resolution of viscous Navier-Stokes problems involving membrane-like structures. As the method is specially tailored for such type of bodies, we firstly give some notes about the implicit representation of geometries, particularly focusing on the level set representation of thin-walled geometries. Secondly, we detail the components of our method by describing the Ausas FE space main features as well as the Nitsche-based imposition of the Navier-slip condition we adopt. Finally, we also present a modified traction calculation formula that partially overcomes the Ausas FE limitations, and thus provides a more suitable drag computation in the context of our proposal.

3.1 | Embedded bodies level set representation

The use of any EBM approach comes with the need of implicitly representing the analysed bodies in the background mesh. This is typically achieved by using a level set method such that the immersed body skin coincides, in an approximate sense, with the zero isosurface of a signed distance function. Depending on the nature of the analysed geometries (with or without well-defined internal volume), the signed distance function can be either continuous or discontinuous.

Hence, those geometries that feature a well-defined internal volume (i.e. volumetric bodies), are commonly represented with a nodal-based continuous level set function, although they can also be represented with a discontinuous one. On the contrary, those bodies with no internal volume (e.g. shell or membrane structures) can only be represented using a discontinuous level set (Fig. 1) as the inside/outside concept required by the continuous level set becomes meaningless in this case.

The enhanced representation capabilities of the discontinuous level set come from the fact that the distance is no longer computed node-wise but element-wise, meaning that the same node can have different distance sign and value depending on the element considered. Although this feature comes at the price of having a potentially discontinuous skin representation, it enables modelling thin-walled immersed bodies, which are otherwise impossible to be represented.

3.2 | Embedded Navier-slip boundary condition for thin-walled bodies

3.2.1 | The Ausas Finite Element space

The Ausas FE space was proposed in[48] and[62] in order to represent the pressure discontinuities arising from the resolution of two phase flow problems. Likewise, it was successfully applied in[63] to model embedded temperature discontinuities. More recently, it has been also used in Navier-Stokes problems to capture the velocity and pressure discontinuities arising from the immersion of an object[47].

Following the ideas presented in[47], the standard FE space is substituted by the Ausas one in all the elements intersected by the level set. At this point, it is important to note that the thin-walled bodies are directly embedded without requiring any interface operation. Such capability comes after the ability of the Ausas FE space to disconnect the solution fields between both level set intersection sides.

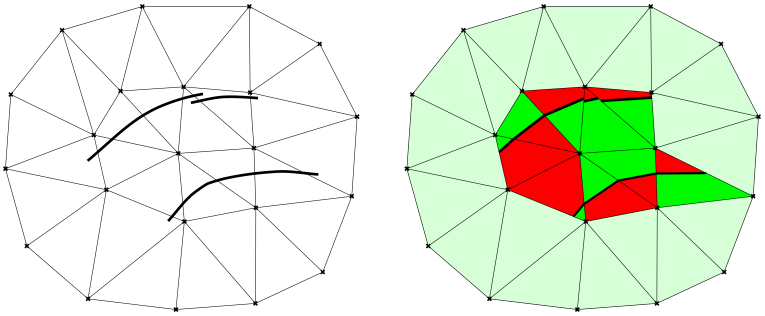

Figure 1 Discontinuous distance function. Body without internal volume (left) and discontinuous distance representation (right). Red and green portions of the cut elements indicate the positive and negative discontinuous distance regions. Light green denotes the non-intersected elements (source[47]).

Moreover, the Ausas FE space is conforming with the standard FE one meaning that no special treatment of the blending elements (i.e. the elements neighbouring the intersected ones) is required. Thanks to this, the formulation remains purely local, something that becomes a great advantage for its extension to distributed memory platforms as no extra communication overhead is introduced.

In the following lines, we summarize the characteristic geometrical features of the Ausas FE space. To do that, we take the same splitting pattern example used by the original authors in[48] (Fig. 2a). After inspecting the shape functions resulting from such splitting configuration (Fig. 2), it can be said that:

- the shape function values are constant along an intersected edge. Hence, N_A takes value one at the green side intersection points Q and P and zero value in the red portion of the element (Fig. 2b). Concerning N_B, it takes value one at the red side intersection point P while it is zero in the green one (Fig. 2c) The same behaviour can be observed for N_C and the intersection point Q (Fig. 2d).
- the previous feature immediately implies that the shape functions values are constant in one of the splitting sides (green one in Fig. 2a) and thus yield a constant interpolation with zero gradient. As a consequence, only piecewise constant functions can be exactly reproduced.
- in the non-constant side, the shape function gradients are approximatively null in the intersection normal direction.

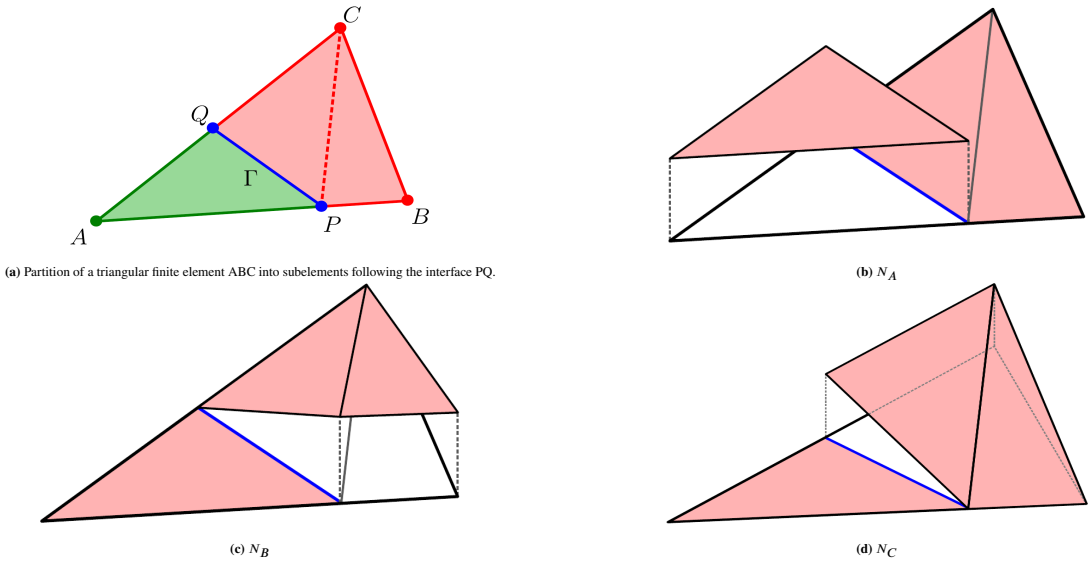

(a) Partition of a triangular finite element ABC into subelements following the interface PQ.

(b) N_A

(c) N_B

(d) N_C

Figure 2 Triangle shape functions for the Ausas finite element space and the splitting pattern in 2a (source[48]).

3.2.2 | Nitsche imposition of the Navier-slip Boundary Condition

This subsection reviews the general Navier-slip BC as well as the Nitsche method we use for its imposition. As it has been already mentioned, our proposal is based on the technique presented by Winter et al. in[44]. Hence, in order to extend its applicability range to thin-walled structures, we adapt such method to be used in combination with the aforementioned Ausas FE space.

The Navier-slip condition can be understood as a wall law whose behaviour is regulated by the so called slip length parameter ε. Denoting the wall velocity as $\mathbf{u}^t$ and the direction normal to the wall as x^n, the Navier-slip condition can be expressed as

$$\varepsilon \frac{\partial \mathbf{u}^t}{\partial x^n} = \mathbf{u}^t \tag{9}$$

From Eq. 9 it can be extracted that the Navier-slip BC approaches the completely stick condition as $\varepsilon \to 0$. Conversely, it tends to the slip limit as $\varepsilon \to \infty$.

From a numerical perspective, the general Navier-slip BC is defined as the combination of a no penetration constraint in the normal direction with a shear force imposition in the tangential one. While the first one is enforced on the normal projection of the velocity, the second is a boundary value imposition of the viscous traction tangential projection, thus implying that the general Navier-skip condition is indeed a Robin-type BC. Taking this into consideration, the general Navier-slip BC can be split in a normal and tangential contribution as

$$\mathbf{P}^n (\mathbf{u} - \mathbf{g}) = \mathbf{0} \tag{10a}$$

$$\mathbf{P}^t \left(\varepsilon \left(\left[\mathbb{C} : (\boldsymbol{\nabla}^s \mathbf{u}) \right] \cdot \mathbf{n} - \mathbf{h} \right) + \mu (\mathbf{u} - \mathbf{g}) \right) = \mathbf{0} \tag{10b}$$

where $\mathbf{g}$ and $\mathbf{h}$ are the corresponding velocity and tangential traction to be imposed over the boundary. $\mathbf{P}^n$ and $\mathbf{P}^t$ are the normal and tangential projection matrices, which can be computed as $\mathbf{P}^n = \mathbf{n} \otimes \mathbf{n}$ and $\mathbf{P}^t = \mathbf{I} - \mathbf{n} \otimes \mathbf{n}$, being $\mathbf{I}$ the 2nd order identity tensor.

The imposition of the BC in Eq. 10 is done by using a stabilized Nitsche method in both the normal and tangential directions. Hence, the Nitsche imposition normal component reads

$$\begin{aligned} \left\langle \frac{\mu}{\gamma h} \left(\mathbf{u}_\mathbf{h} - \mathbf{g} \right) \mathbf{P}^n, \mathbf{w} \right\rangle_\Gamma - \left\langle \left(\mathbf{u}_\mathbf{h} - \mathbf{g} \right) \mathbf{P}^n, (q\mathbf{I} + \zeta \mathbb{C} : \boldsymbol{\nabla}^s \mathbf{w}) \, \mathbf{n} \right\rangle_\Gamma + \\ \left\langle \frac{\phi_u}{\gamma h} \left(\mathbf{u}_\mathbf{h} - \mathbf{g} \right) \mathbf{P}^n, \mathbf{w} \right\rangle_\Gamma \end{aligned} \tag{11}$$

while the tangential one is

$$\begin{aligned} \left\langle \frac{1}{\varepsilon + \gamma h} \left(\varepsilon \left(\mathbb{C} : \boldsymbol{\nabla}^s \mathbf{u}_\mathbf{h} \mathbf{n} - \mathbf{h} \right) + \mu \left(\mathbf{u}_\mathbf{h} - \mathbf{g} \right) \right) \mathbf{P}^t, \mathbf{w} \right\rangle_\Gamma - \\ \zeta \left\langle \frac{\gamma h}{\varepsilon + \gamma h} \left(\varepsilon \left(\left[\mathbb{C} : \left(\boldsymbol{\nabla}^s \mathbf{u}_\mathbf{h} \right) \right] \cdot \mathbf{n} - \mathbf{h} \right) + \mu \left(\mathbf{u}_\mathbf{h} - \mathbf{g} \right) \right) \mathbf{P}^t, (\boldsymbol{\nabla}^s \mathbf{w}) \cdot \mathbf{n} \right\rangle_\Gamma \end{aligned} \tag{12}$$

in which γ is a penalty constant and $\zeta \in \{-1, 1\}$. The choice of $\zeta = -1$ leads to the adjoint inconsistent Nitsche formulation, which enjoys improved *inf-sup* stability for any value of the penalty constant[44]. Even though optimal convergence is not guaranteed for the velocity L^2-error in this case, we opt to use the adjoint inconsistent formulation owing to its reported better stability properties. ϕ_u is a stabilization constant defined as

$$\phi_u = \mu + \rho \|\mathbf{u}\| h + \frac{\rho}{\Delta t} h^2 \tag{13}$$

At this point, it needs to be clearly stated that these two constraints need to be integrated in both sides of the level set interface. This is a direct consequence of the modification of the standard FE space by the Ausas one inside the intersected elements, which makes the positive and negative sides solution completely independent. Therefore, the problem somehow turns into imposing the same Nitsche-based constraints in two overlapping but different interfaces.

We note that the choice of using the Ausas FE space inherently reduces the approximation properties of the space within the cut elements, so exactly where the Nitsche terms are active. This effect might be particularly relevant since, depending on the cut structure, the gradient of the velocity and of the test function are kinematically forced to be zero in one of the sides of the cut. It is thus important to verify that the Navier-slip BC is still correctly enforced despite such kinematic limitation. This is done by numerical verification in the examples section.

3.2.3 | Drag calculation

This short section derives a more suitable expression for the drag calculation when the Ausas FE space is used in combination with a Navier-slip BC. Hence, we start from the application of the previously defined projection operators $\mathbf{P}^n$ and $\mathbf{P}^t$ to the viscous component of the Cauchy traction vector. This simple operation allows to split the viscous drag in two components as

$$\mathbf{t} = \mathbf{P}^n \left((\mathbb{C} : \boldsymbol{\nabla}^s \mathbf{u}) \cdot \mathbf{n} \right) + \mathbf{P}^t \left((\mathbb{C} : \boldsymbol{\nabla}^s \mathbf{u}) \cdot \mathbf{n} \right) - p\mathbf{n} \tag{14}$$

Furthermore, we consider that the Navier-slip BC requires the traction parallel to the wall $t_{\parallel}$ to be $t_{\parallel} = -\frac{\mu}{\varepsilon}\mathbf{P}^t(\mathbf{u}-\mathbf{g})$, or equivalently that $\mathbf{P}^t \left(\left(\mathbb{C} : \boldsymbol{\nabla}^s \mathbf{u} \right) \cdot \mathbf{n} \right) \approx -\frac{\mu}{\varepsilon}\mathbf{P}^t(\mathbf{u}-\mathbf{g})$. This can be used to rewrite Eq.14 in the alternative form

$$\mathbf{t} \approx \mathbf{P}^n \left((\mathbb{C} : \boldsymbol{\nabla}^s \mathbf{u}) \cdot \mathbf{n} \right) - \frac{\mu}{\varepsilon}(\mathbf{u}-\mathbf{g})\mathbf{P}^t - p\mathbf{n} \tag{15}$$

The original and the alternative expressions are equivalent in the continuum and when a "standard" FE formulation is employed. However, this no longer holds when the Ausas FE is introduced since in presence of zero velocity gradients the original expression would predict a zero skin friction while the alternative one correctly estimates the skin friction whenever the tangential velocity is nonzero on the cut boundary, even when the gradient is zero in the immediate vicinity of the cut.

In order to explain such inconsistency, we need to take into account that the use of Ausas FE space can be interpreted as the use of the standard FE space subjected to an additional constraint that enforces the solution to be piecewise constant along each cut edge. The action of such geometric constraint is fundamental for the way in which equilibrium is established in the vicinity of the immersed objects. Indeed, the action of the Ausas FE geomeetric constraint allows forces to be transmitted from the cut boundary to the surrounding nodes without the need of introducing a gradient in the solution, and is the reason for which the effective tangential stress can be nonzero around the immersed boundaries.

The practical implication is that, as we shall show in the validation section, only the use of Eq. 15 delivers correct traction predictions when the Ausas FE space is employed.

4 | VALIDATION

This section collects the benchmarking of the proposed formulation. To ensure that all the proposed examples can be reproduced, we detail the geometry, BCs and simulation settings prior to the discussion of the results.

In the following we list and motivate the choice of the examples:

- 2D straight channel: to check the implementation and convergence rates of the formulation.
- 2D flow inside a ring: to obtain the convergence rates of the formulation when dealing with faceted approximations of curved geometries. The influence of the Nitsche constant γ is also evaluated with this example.
- 2D flow around pressurized cylinder: to prove the utility of the pseudo-compressible term when isolated fluid cavities appear.
- 2D elbow with internal wall: to test the performance, including matrix ill-conditioning, of the formulation against alternative embedded approaches.
- 2D flow around thin-walled arch profile: to assess the capability of the proposed technique to solve high Reynolds number (Re) flows. This example is conceived as a 2D idealization of the final 3D example.
- 3D flow around a sailboat: to show a potential industrial application of the proposed formulation.

4.1 | 2D straight channel

The objective of this first example is to preliminary assess the correctness and convergence rates of the proposed formulation. Thus, the geometry and boundary conditions have been selected to be as simple as possible.

The geometry consists in a 2D 1.1x2m straight rectangular channel. The discontinuous level set function is set such that the effective width of the channel is 1m. Regarding the wall behaviour, the bottom edge is considered as a no-slip boundary while the embedded top one is tested with a slip and no-slip BCs. Moreover, we also solve an extra intermediate case in which the embedded skin ε equals 10^{-1}m.

Regarding the material properties, they are set to yield a *Re* equal to 100. This is achieved by setting the density to 1kg/m^3 and the viscosity to 1e-2kg/ms.

A second order Backward Differentiation Formula (BDF2) scheme is used for the time discretization. To ensure that the steady state solution is reached, 20 time steps of 100s (Δt) are run.

The problem is solved for a set of structured meshes. The characteristic element size and edge subdivisions of each one of the refinement levels are collected in Table 1.

Table 1 2D straight channel mesh refinement settings.

	Mesh 0	Mesh 1	Mesh 2	Mesh 3	Mesh 4	Mesh 5
Element size [m]	0.2	0.0667	0.0333	0.0016	0.0083	0.0042
Short edge divisions	5	15	30	65	120	241
Long edge divisions	10	30	60	130	240	480

4.1.1 | Slip interface

In this case the flow is induced by applying a volume force of 0.5m/s^2 in the horizontal direction This drives the solution to a steady state that can be characterized by the following rigid body movement

$$v_x = 50y\left(1 - \frac{y}{2}\right) \tag{16a}$$

$$v_y = 0 \tag{16b}$$

$$p = 0 \tag{16c}$$

Table 2 collects the $L^2\,(\Omega)$-norm of both the velocity and pressure errors. Figs. 3a and 3b depict the previous results. As it can be observed, the convergence order is $O(h^2)$ for the velocity field while it is superlinear for the pressure one.

We observe that the obtained convergence rates match those expected for linear FE, even though the Ausas FE space is limited to $O(h^{3/2})$[48]. This is a particularity of the current test case, which presents the maximum velocity at the top embedded boundary. As a consequence, the solution gradient in this region tends to zero as the mesh is refined, thus implying that the zero-gradient limitation of the Ausas FE space does not show up in this case.

Finally, Fig. 4 shows the velocity field for different refinement levels (meshes 1, 3 and 5 in Table 1). It can be observed that the obtained solutions match the parabolic rigid body movement in Eq. 16a.

Table 2 2D straight channel. Velocity and pressure error norms (slip interface).

	Mesh 0	Mesh 1	Mesh 2	Mesh 3	Mesh 4	Mesh 5
$\|\mathbf{u} - \mathbf{u_h}\|_{L^2(\Omega)}$	2.41253	0.950292	0.129366	0.007083	0.001888	0.000479
$\|p - p_h\|_{L^2(\Omega)}$	0.056811	0.009313	0.001444	0.000376	0.000144	0.000051

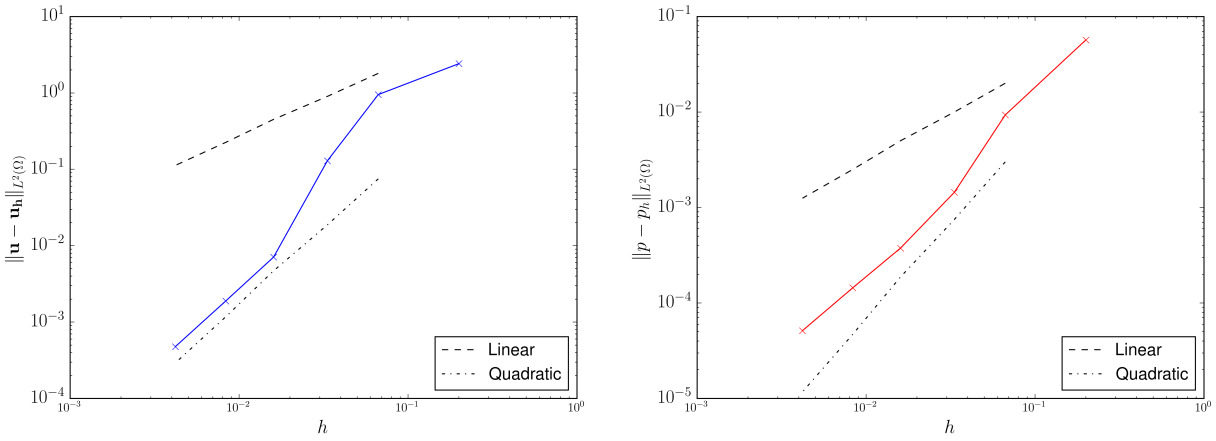

(a) Velocity convergence.

(b) Pressure convergence.

Figure 3 2D straight channel (slip interface). Velocity and pressure error norms convergence.

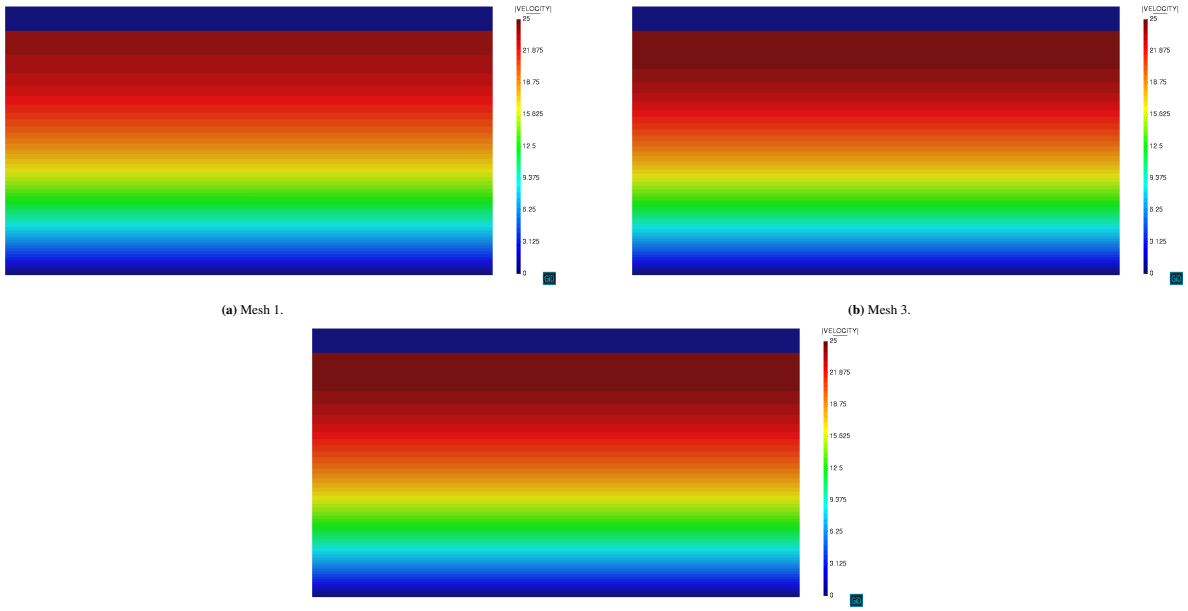

(a) Mesh 1.

(b) Mesh 3.

(c) Mesh 5.

Figure 4 2D straight channel (slip interface). Coarse, intermediate and fine meshes velocity field.

4.1.2 | No-slip interface

In this case we introduce a pressure gradient between the inlet and the outlet instead of using a body force to induce the flow. Thus, the pressure is fixed to 1Pa in the left edge and to 0Pa in the right one. This, in combination with the no-slip BC in the top edge, leads to the well known pressure driven flow between two steady plates benchmark, also known as Poiseuille flow. The steady state analytical solution of the Poiseuille flow, particularised for the above mentioned material properties, can be computed as

$$v_x = 25\,[y\,(1-y)] \tag{17a}$$

$$v_y = 0 \tag{17b}$$

$$p = \frac{2-x}{2} \tag{17c}$$

Table 3 collects the $L^2(\Omega)$-norm of the velocity and pressure errors. The results exhibit a convergence rate around $O(h)$ for both velocity and pressure fields (Figs. 5a and 5b).

Fig. 6 depicts the solution fields for different mesh refinement levels (meshes 1, 3 and 5 in Table 1). The expected parabolic velocity profile and linear pressure gradient is obtained in all cases. Furthermore, it is worth commenting about the perturbations appearing close to the embedded boundary, which can be clearly observed in the coarser mesh pressure field (Fig. 5b). These are direct consequence of the inability of the Ausas FE space to represent the gradient in one of the two sides of an intersected element. Taking into account that the side in which the constant interpolation occurs depends on the intersection pattern, these oscillations are totally expected.

Table 3 2D straight channel. Velocity and pressure error norms (no-slip interface).

	Mesh 0	Mesh 1	Mesh 2	Mesh 3	Mesh 4	Mesh 5
$\|\mathbf{u}-\mathbf{u_h}\|_{L^2(\Omega)}$	3.1982	1.06859	0.28365	0.07003	0.035238	0.014591
$\|p-p_h\|_{L^2(\Omega)}$	0.067731	0.02977	0.012579	0.004407	0.001754	0.000556

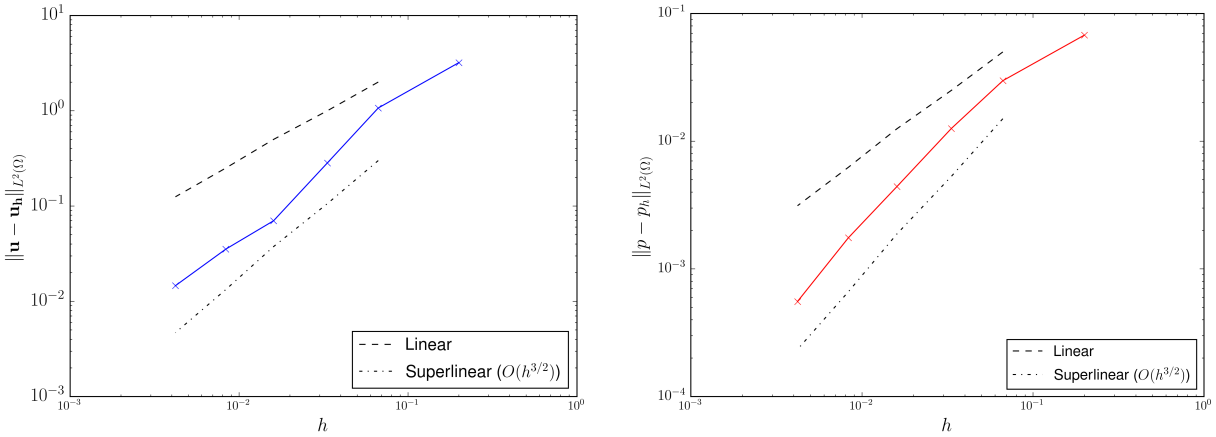

(a) Velocity convergence.

(b) Pressure convergence.

Figure 5 2D straight channel (no-slip interface). Velocity and pressure error norms convergence.

4.1.3 | Slip length 10^{-1} interface

With this last variant of the straight channel example we aim to test the performance of the proposed technique when it is used in a wall law fashion. This means to introduce a controlled wall friction such that the embedded boundary behaviour is somehow in between the slip and no-slip limits. Hence, we solve the same geometry but setting the slip length ϵ to 10^{-1}. The inlet profile $v_x = 1-(1/(1+\epsilon))y$ is imposed in the left edge. Besides, the bottom edge velocity is fixed to [1,0]m/s.

These settings yield the analytical velocity and pressure steady state solution

$$v_x = 1 - \left(\frac{1}{1+\epsilon}\right) y \tag{18a}$$

$$v_y = 0 \tag{18b}$$

$$p = 0 \tag{18c}$$

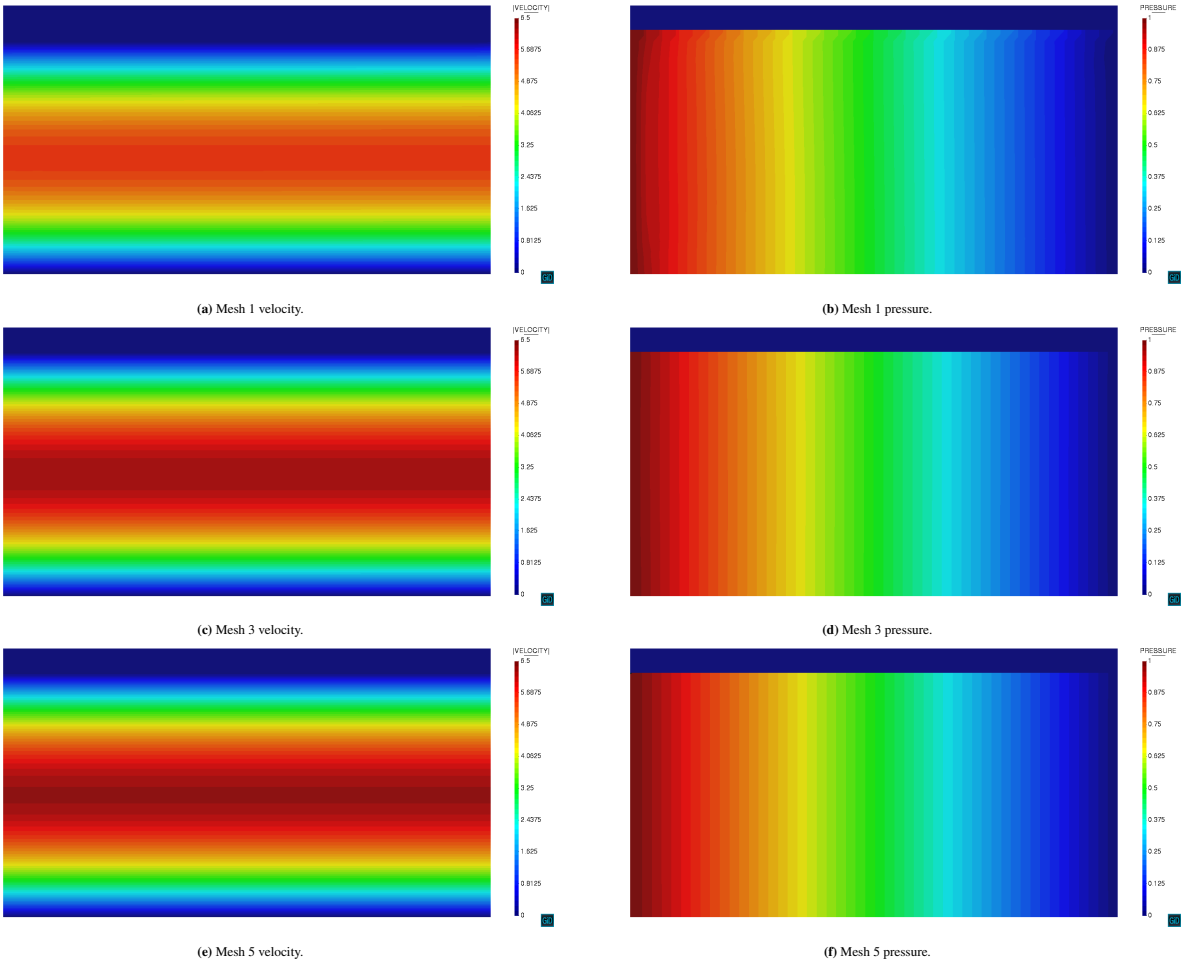

(a) Mesh 1 velocity.

(b) Mesh 1 pressure.

(c) Mesh 3 velocity.

(d) Mesh 3 pressure.

(e) Mesh 5 velocity.

(f) Mesh 5 pressure.

Figure 6 2D straight channel (no-slip interface). Coarse, intermediate and fine meshes solutions.

from which a total drag force equal to 0.0182N is obtained in the top embedded boundary.

Table 4 collects the L^2 (Ω)-norm of both the velocity and pressure errors as well as the L^2 (Γ)-norm of the horizontal drag force error for three different values of the penalty constant γ. As it can be observed in Fig. 7, the convergence rate of the three analysed magnitudes is around $O(h)$, which is in line with the previous pure no-slip results. We also note that the convergence rate of the formulation is not affected by the γ value. Besides that, the error constant minimizes for higher *gamma* values as it could be expected. Complementary, Fig. 8 shows that the obtained velocity field agrees the linear analytical one in the three refinement levels (Meshes 1, 3 and 5 in Table 1).

4.2 | 2D flow inside a ring

It is known that the imposition of BCs over faceted approximations of curved boundaries can be problematic, specially when a pure slip wall behaviour needs to be modelled[43]. This is explained by the fact that the slip BC intrinsically requires the velocity to be parallel to each face of the discrete polygonal approximation. In consequence, the unique wall solution that fulfils such requirement in the vertices that are shared among different faces is the null velocity. As it is described in[43] and[47], this can lead to a wrong null velocity approximation in the slip boundary, which likely appears when the curved boundaries are discretized too coarse.

This test aims to assess and evaluate the convergence rates of the formulation in such curved boundaries polygonal approximations scenario. Similar to what is done in[43], we set a simple 2D geometry that consists of two concentric cylinders separated by an interior fluid cavity. The inner cylinder radius is 0.5m while the outer one is 1.0m, meaning that the computational domain

Table 4 2D straight channel. Velocity and pressure error norms (slip length 10^{-1}m interface).

		Mesh 0	Mesh 1	Mesh 2	Mesh 3	Mesh 4	Mesh 5
$\gamma = 10^{-1}$	$\|\mathbf{u} - \mathbf{u_h}\|_{L^2(\Omega)}$	0.026176	0.008904	0.001587	8.78378e-05	4.5824e-05	2.21285e-05
	$\|p - p_h\|_{L^2(\Omega)}$	0.015735	0.005540	0.000865	3.40915e-05	1.56027e-05	9.09062e-06
	$\|f - f_{x_h}\|_{L^2(\Gamma)}$	0.034265	0.023253	0.019279	0.018424	0.018315	0.018247
$\gamma = 10^{-2}$	$\|\mathbf{u} - \mathbf{u_h}\|_{L^2(\Omega)}$	0.027379	0.009778	0.002054	0.00023	0.000162	8.08048e-05
	$\|p - p_h\|_{L^2(\Omega)}$	0.019098	0.006327	0.001165	0.000164	8.69214e-05	4.38793e-05
	$\|f - f_{x_h}\|_{L^2(\Gamma)}$	0.033049	0.022813	0.019053	0.018319	0.018256	0.018219
$\gamma = 10^{-3}$	$\|\mathbf{u} - \mathbf{u_h}\|_{L^2(\Omega)}$	0.027548	0.009871	0.002102	0.000322	0.000174	8.67592e-05
	$\|p - p_h\|_{L^2(\Omega)}$	0.019457	0.006407	0.001196	0.000177	9.52864e-05	4.74011e-05
	$\|f - f_{x_h}\|_{L^2(\Gamma)}$	0.032919	0.022768	0.01903	0.018308	0.01825	0.018216

Ω can be described as $(x, y) \in \mathbb{R}^2 : \ 0.25 \leq x^2 + y^2 \leq 1$. The fluid is initially at rest and a unit angular velocity $\bar{v}_\Theta$ is imposed in the outer cylinder to induce the flow. The pressure is fixed to zero along the outer cylinder edge.

With regard to the material properties, the dynamic viscosity μ and density ρ are 1.0kg/m^3 and 1e-3kg/ms, respectively. A second order BDF2 scheme is used for the time discretization. To ensure that the steady state solution is reached, 10 time steps of 200s (Δt) are solved.

A centred structured mesh is used in all the refinement levels of the study. Note that the outer cylinder is completely meshed disregarding the inner one, which is represented by a radial discontinuous distance function. The characteristic element size together with the number of radial and perimeter subdivisions are collected in Table 5. Fig. 9 shows the mesh defined as Mesh 1 in Table 5. More specifically, Fig. 9a depicts the centred structured pattern while Fig. 9b does so for the distance function intersection pattern.

In the following, we study the convergence of the obtained solution when slip and no-slip BC are imposed in the inner boundary.

Table 5 2D flow inside a ring mesh refinement settings.

	Mesh 0	Mesh 1	Mesh 2	Mesh 3	Mesh 4	Mesh 5	Mesh 6
Element size [m]	0.1428	0.06667	0.03448	0.01754	0.00884	0.00444	0.00223
Radial divisions	7	15	29	57	113	225	449
Perimeter divisions	21	43	85	169	337	673	1345

4.2.1 | Slip interface

In all the cases presented in this subsection, the slip length ε has been set to 10^8, which is a large enough value to ensure a slip-like behaviour. The Nitsche penalty constant γ has been set to 0.1 in all the examples. The slip interface analytical solution can

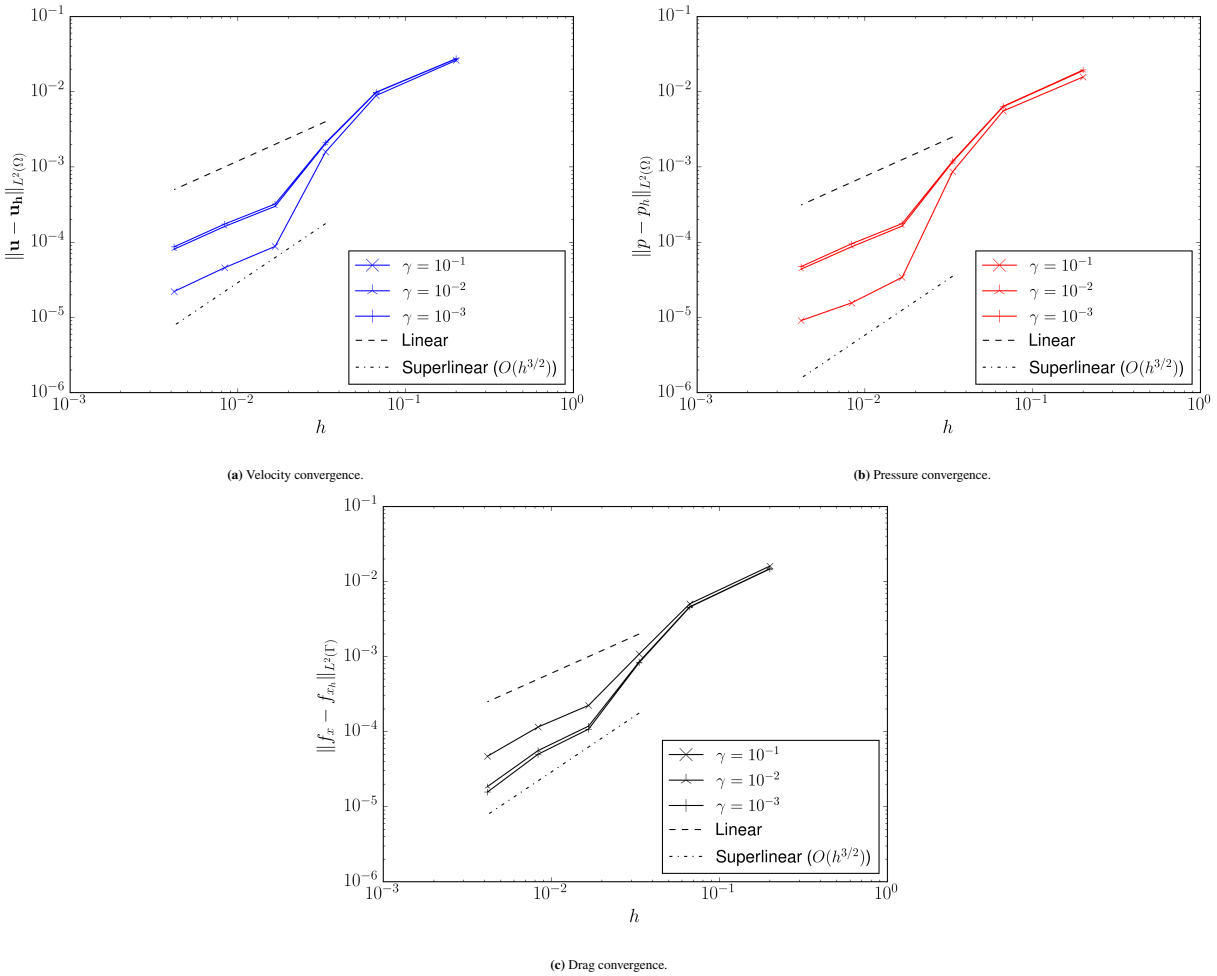

(a) Velocity convergence.

(b) Pressure convergence.

(c) Drag convergence.

Figure 7 2D straight channel (slip length 10^{-1}m interface). Velocity and pressure error norms convergence.

be expressed in polar coordinates as

$$v_r = 0 \tag{19a}$$

$$v_\Theta = r \tag{19b}$$

$$p = \frac{\rho}{2}\left(r^2 - 1\right) \tag{19c}$$

Table 6 collects the $L^2(\Omega)$-norm of the velocity and pressure errors. Fig. 10a and Fig. 10b display a superlinear convergence rate close to $O(h^{3/2})$ for both the velocity and the pressure fields. These results are in line with the ones reported in[48] and[47].

The obtained velocity and pressure fields are shown for three of the refinement levels (Mesh 0, 3 and 6) in Fig. 11. It can be easily noted that the coarsest mesh solution is far from the expected slip behaviour. Nevertheless, the method manages to properly capture the slip solution as the mesh is refined. These results are in agreement with the ones reported in[43] for the resolution of a similar Stokes problem using a Nitsche slip BC imposition.

Having said this, we believe that the deterioration of the convergence rates is mainly due to the combination of a weak imposition of the slip BC with the polygonal approximation of curved boundaries.

Complementary, we also test the penalty constant γ sensitivity when $\varepsilon \to \infty$ by solving the same example but using the finest mesh and a set of γ values ranging from from 10^{-4} to 10^{2}. The $L^2(\Omega)$-norms of the velocity and pressure errors are collected in Table 7 and depicted in Fig. 12 for all γ values. It can be observed that both error norms reach their minimum for γ values between 0.1 and 10, being the infimum values around the unit γ value.

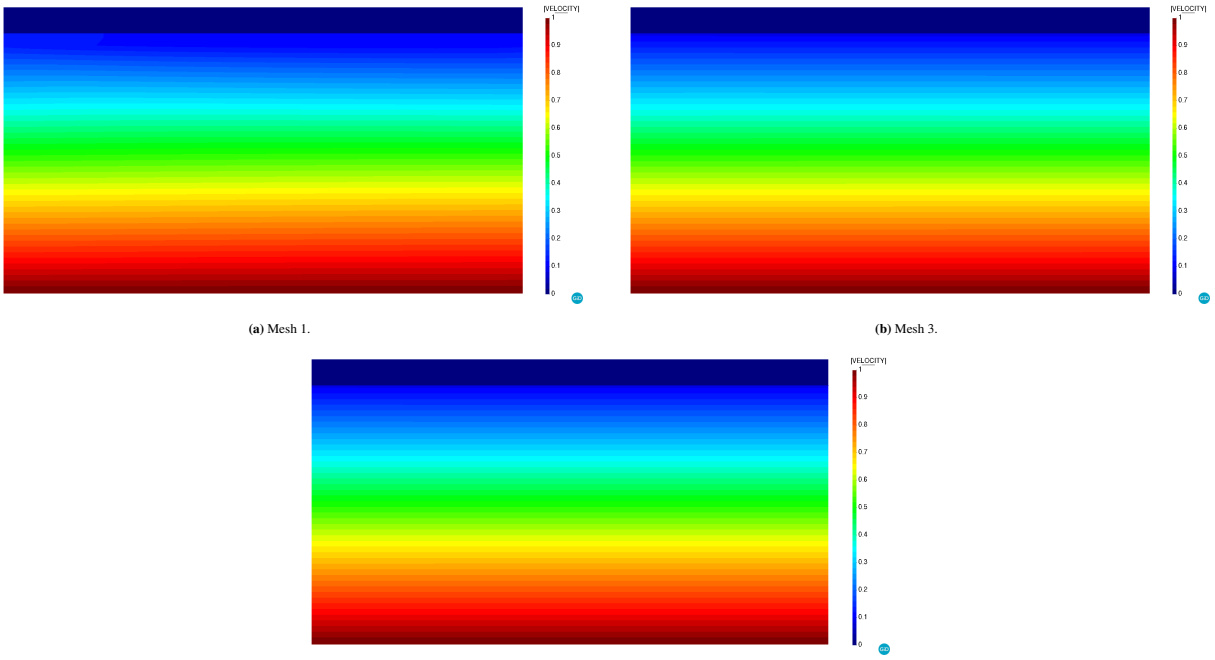

(a) Mesh 1.

(b) Mesh 3.

(c) Mesh 5.

Figure 8 2D straight channel (slip length 10^{-1}m interface). Coarse, intermediate and fine meshes velocity field.

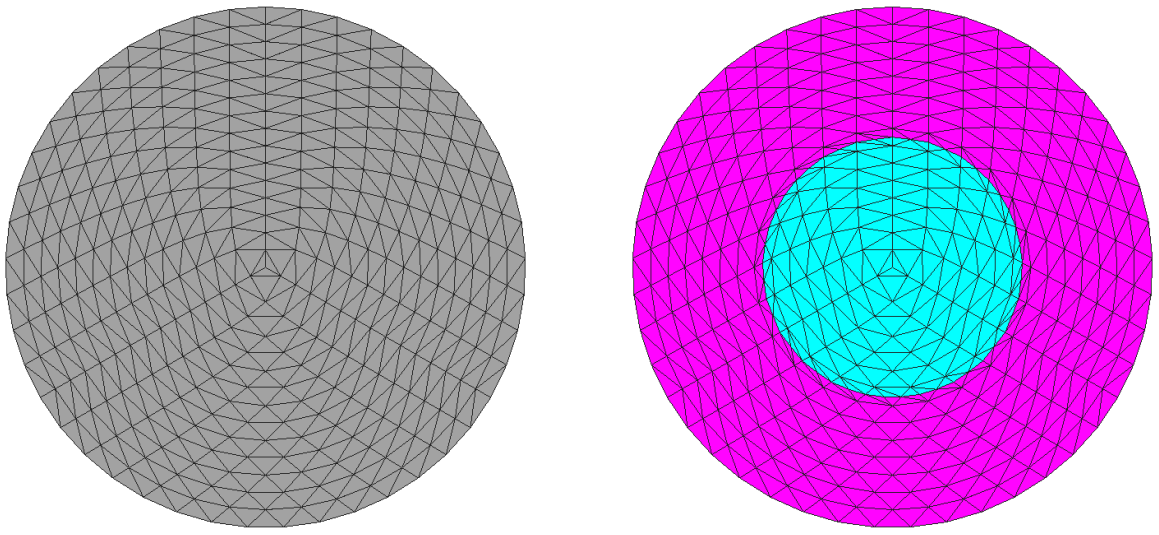

(a) Mesh capture.

(b) Distance intersection pattern.

Figure 9 2D flow inside a ring. Test case geometry (Mesh 1).

4.2.2 | No-slip interface

In this case the slip length ϵ is set to 0m to enforce a no-slip behaviour in the embedded interface. The Nitsche penalty constant γ is kept as 0.1. As in the slip case, the results and convergence assessment are based on the analytical solution, which in in

Table 6 2D flow inside a ring (slip interface). Velocity and pressure error norms.

	Mesh 0	Mesh 1	Mesh 2	Mesh 3	Mesh 4	Mesh 5	Mesh 6
$\|\mathbf{u}-\mathbf{u_h}\|_{L^2(\Omega)}$	0.372217	0.265875	0.173553	0.092081	0.040315	0.016052	0.006761
$\|p-p_h\|_{L^2(\Omega)}$	0.148217	0.084728	0.055737	0.030523	0.013681	0.005508	0.002329

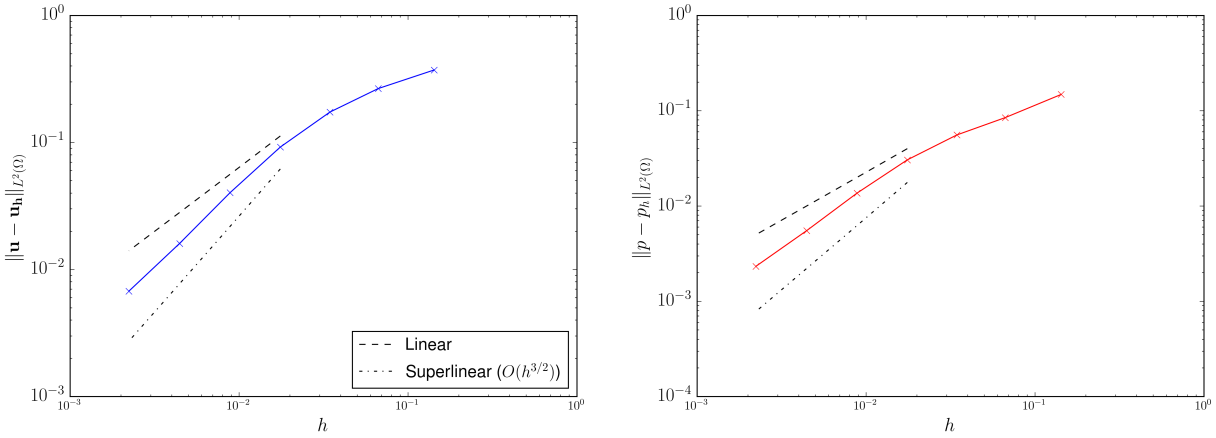

(a) Velocity convergence.

(b) Pressure convergence.

Figure 10 2D flow inside a ring (slip interface). Velocity and pressure error norms convergence.

Table 7 2D flow inside a ring (slip interface). Velocity and pressure error norms for different values of the penalty factor γ.

γ	1.0e+2 0	1.0e+1	1.0e+0	1.0e-1	1.0e-2	1.0e-3	1.0e-4
$\|\mathbf{u}-\mathbf{u_h}\|_{L^2(\Omega)}$	0.066914	0.010858	0.003796	0.006761	0.03991	0.183505	0.319047
$\|p-p_h\|_{L^2(\Omega)}$	0.022297	0.003725	0.0013086	0.002329	0.013493	0.057347	0.092092

polar coordinates reads as

$$v_r = 0 \tag{20a}$$

$$v_\Theta = \frac{\bar{v}_\Theta}{1-0.5^2}\left(\frac{r^2-0.5^2}{r}\right) \tag{20b}$$

$$p = \frac{\bar{v}_\Theta \rho}{2(1-0.5^2)^2}\left(r^2 - log(r) - \frac{0.5^2}{r^2} - 0.9375\right) \tag{20c}$$

Table 8 $L^2(\Omega)$-norms of the velocity and pressure errors. These results are also depicted in Figs. 10a and 10b, which exhibit a linear convergence rate for both velocity and pressure fields. Such deterioration of the convergence rates is associated to the inability of the Ausas FE space to capture the shear effects in some of the intersected elements. Finally, we show in Fig. 11 the solution for three of the refinement levels (Meshes 0, 3 and 6). It can be observed that the solution tends to the analytical one as the mesh is refined.

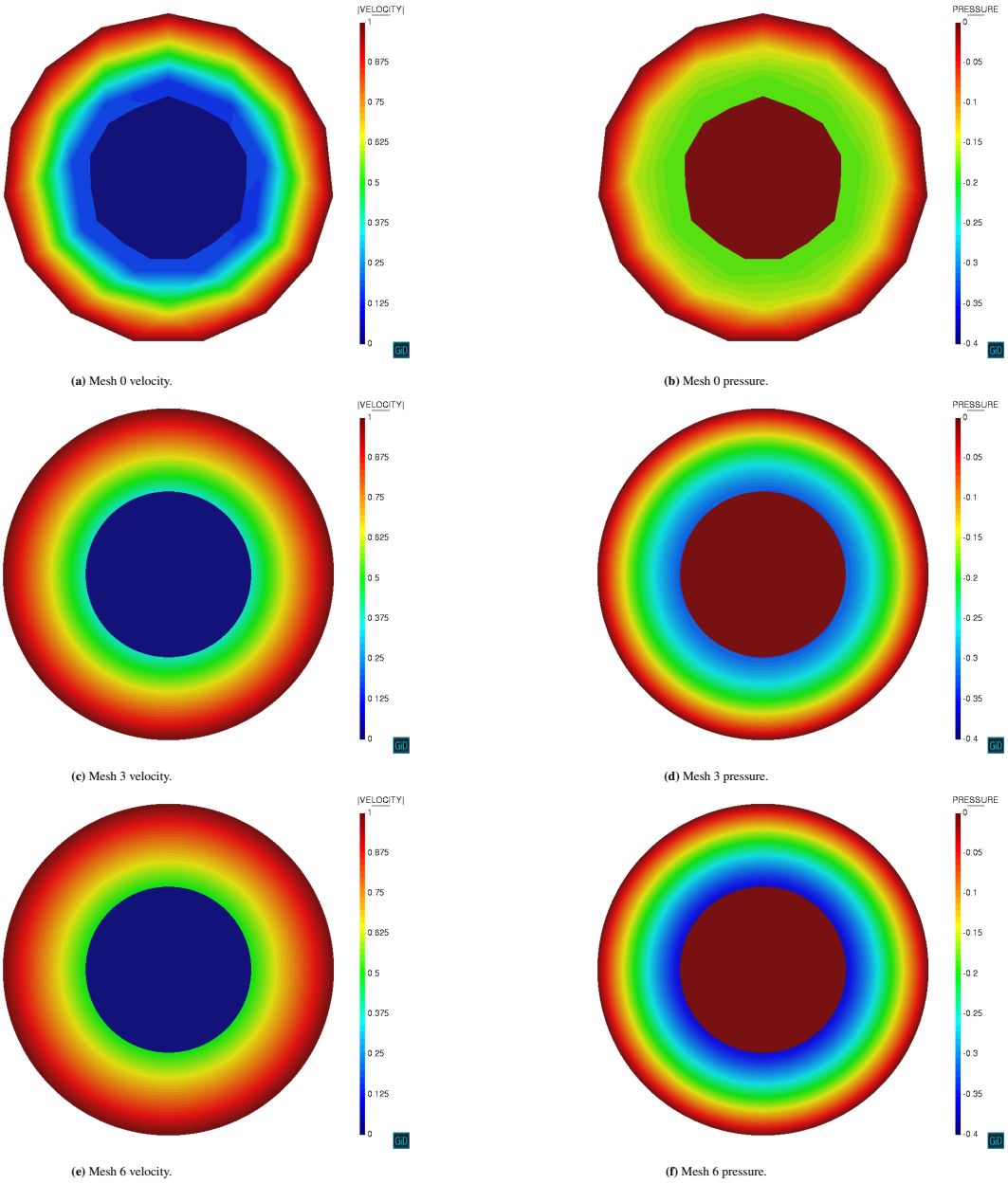

(a) Mesh 0 velocity.

(b) Mesh 0 pressure.

(c) Mesh 3 velocity.

(d) Mesh 3 pressure.

(e) Mesh 6 velocity.

(f) Mesh 6 pressure.

Figure 11 2D flow inside a ring (slip interface). Coarsest, intermediate and finest meshes solutions.

4.3 | 2D flow around pressurized cylindrical membrane

This example is specifically conceived to prove the capability of the pseudo-compressible term in Eq. 2b to prevent the pressure field to blow up when isolated cavities of fluid appear.

Hence, we solve the fluid flow around an embedded cylindrical membrane that is represented by a discontinuous level set function. Thanks to the ability of the Ausas FE space to disconnect both sides of the level set, the embedded cylinder becomes an isolated fluid cavity with no pressure constraint, thus requiring the addition of an extra pseudo-compressibility term in order to keep the pressure bounded.

The problem geometry consists in a 1x5m straight channel. A 0.1m radius cylinder centred in the (1.25,0.5)m coordinates is placed inside the channel. With regard to the fluid properties, we set ρ and μ to 1.0kg/m^3 and 1e-2kg/ms. The speed of sound velocity c is equal to 1e3m/s, which is a feasible value for a liquid. A volume force $\mathbf{b}$ equal to $[0.0, -10.0]$m/s^2 is considered

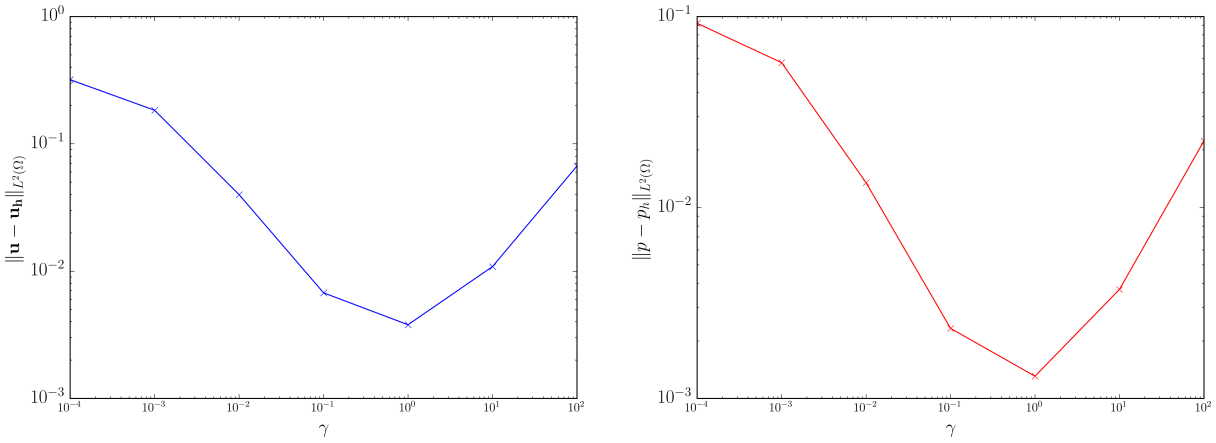

(a) Velocity error norm.

(b) Pressure error norm.

Figure 12 2D flow inside a ring (slip interface). Error norms for different γ values.

Table 8 2D flow inside a ring (no-slip interface). Velocity and pressure error norms.

	Mesh 0	Mesh 1	Mesh 2	Mesh 3	Mesh 4	Mesh 5	Mesh 6
$\|\mathbf{u}-\mathbf{u_h}\|_{L^2(\Omega)}$	0.083878	0.047655	0.024639	0.012780	0.006550	0.003318	0.001670
$\|p-p_h\|_{L^2(\Omega)}$	0.055474	0.015289	0.006531	0.003074	0.001510	0.000751	0.000374

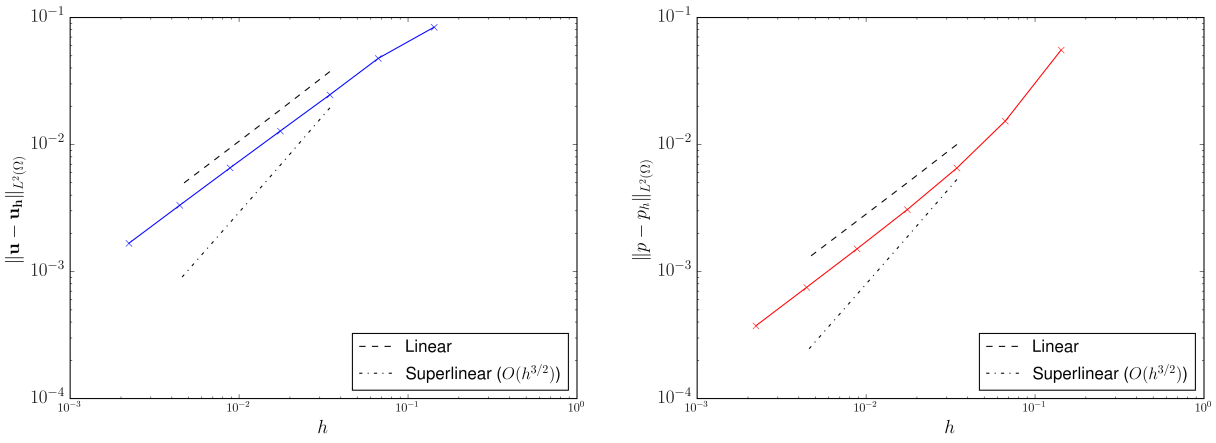

(a) Velocity convergence.

(b) Pressure convergence.

Figure 13 2D flow inside a ring (no-slip interface). Velocity and pressure error norms convergence.

inside the cylinder (Figs. 15a and 15b) so to ensure that the initial solution inside the cylinder (zero velocity and pressure) is not in equilibrium.

A constant inlet velocity profile of 1m/s is imposed in the left edge of the channel. Furthermore, a symmetry condition (zero normal velocity and free tangential velocity) is enforced in the top and bottom walls. In order to get a steady state solution, we model the cylinder as a slip body by setting ϵ to 1e8m. We remark that the pressure is not fixed in any point of the computational domain.

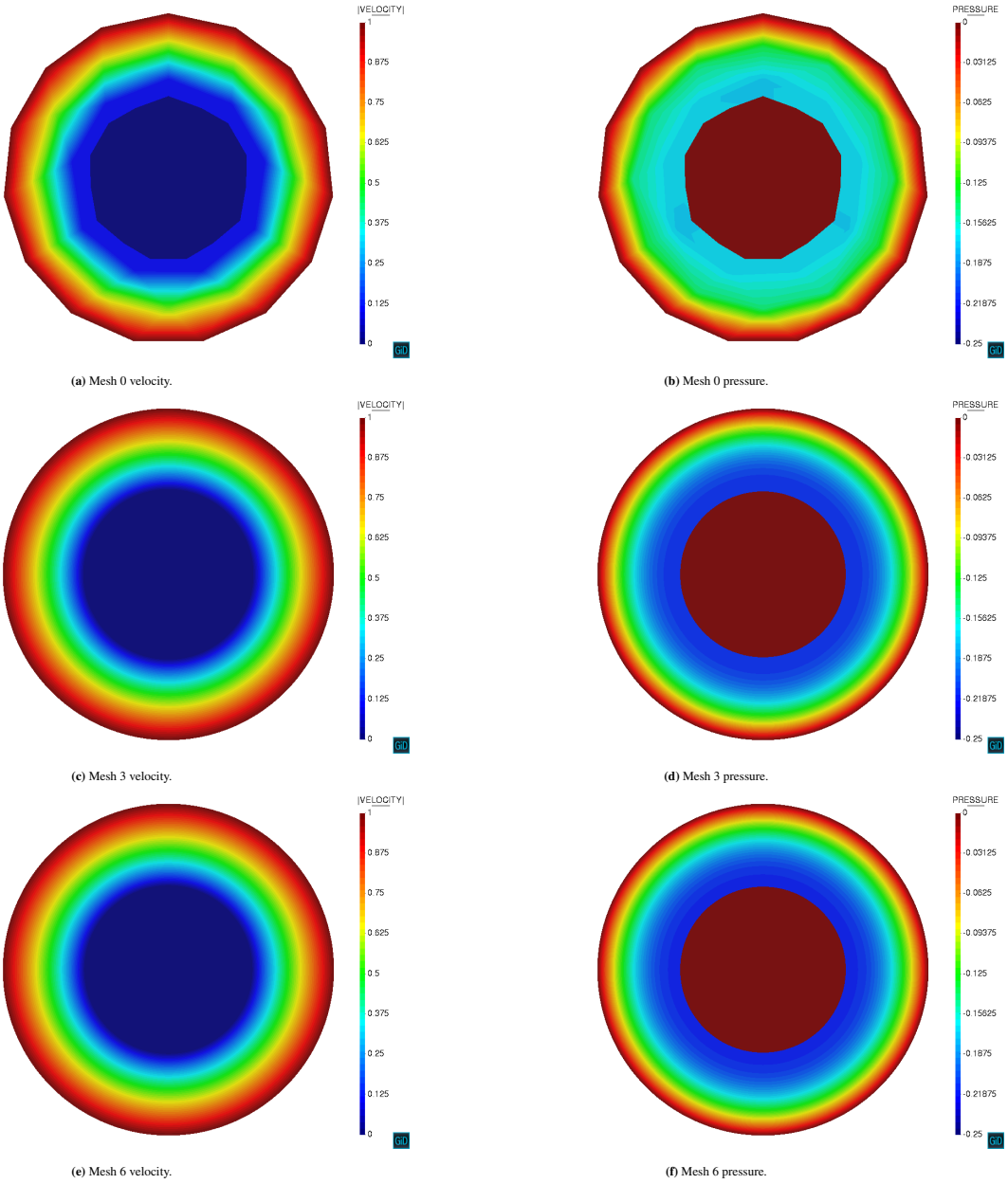

(a) Mesh 0 velocity.

(b) Mesh 0 pressure.

(c) Mesh 3 velocity.

(d) Mesh 3 pressure.

(e) Mesh 6 velocity.

(f) Mesh 6 pressure.

Figure 14 2D flow inside a ring (no-slip interface). Coarsest, intermediate and finest meshes solutions.

The time discretization is done using a BDF2 scheme with a constant time step equal to 1s. To ensure that the steady solution is reached, we simulate a total time of 100s. The channel is meshed with a structured grid made of around 200k linear triangular elements, whose average size is 7e-3m.

Figs. 15c and 15e depict the obtained solution. As expected, the flow around the cylinder presents an upstream stagnation point and a symmetric steady wake. Inside the cylinder (Fig. 15d and 15f), the hydrostatic pressure distribution can also be clearly identified. These results prove that, provided a suitable initial condition, the addition of a weak compressibility is sufficient to keep the pressure bounded, and therefore to ensure convergence, despite the presence of isolated fluid cavities with no pressure constraint.

Finally, we would like to spend some words on the relevance that these results have for the application of the proposed technique to real life problems involving “dirty” input geometries. Although in this case the unbounded pressure issue can be readily patched by fixing the pressure in any point inside the cylinder, this is likely impossible to be done in a real scenario since complex geometries can be rarely described using an analytical level set functions as the one we use for the cylinder. In this

context, the introduction of the weak compressibility term guarantees the applicability of the proposed formulation to complex scenarios (e.g. real geometries or complex moving domains) as it makes possible to automatically handle such unbounded pressure cavities with an “a priori” unknown location.

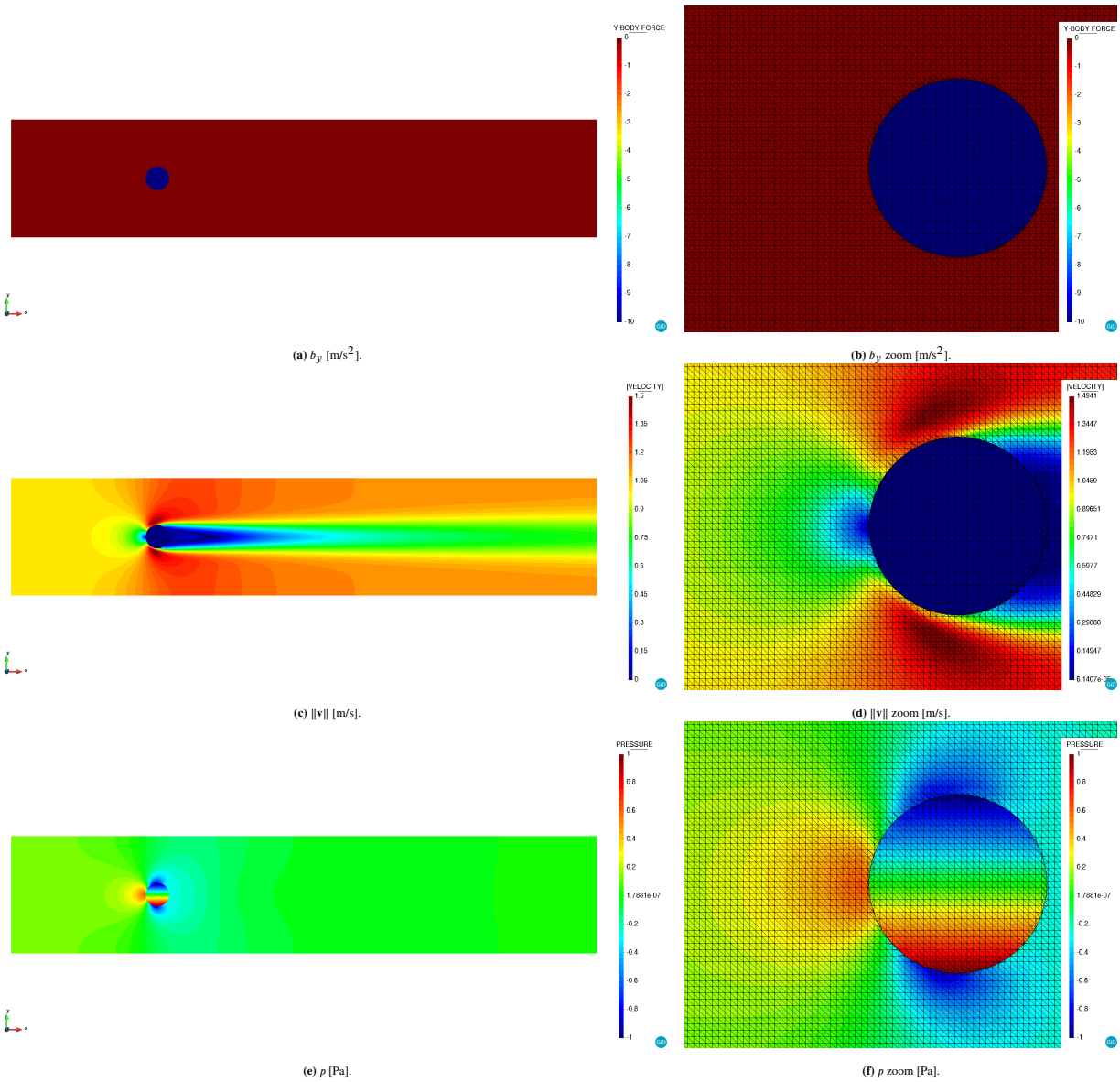

(a) b_y [m/s^2]. **(b)** b_y zoom [m/s^2]. **(c)** $\|\mathbf{v}\|$ [m/s]. **(d)** $\|\mathbf{v}\|$ zoom [m/s]. **(e)** p [Pa]. **(f)** p zoom [Pa].

Figure 15 2D flow around pressurized cylindrical membrane. Body force, $\|\mathbf{v}\|$ and p fields for c 1e3m/s. In the left hand side a general view of the entire domain is presented. In the right hand side a zoom of the cylinder region is shown together with the background mesh, which includes the intersected elements subdivisions used for the subintegration.

4.4 | 2D elbow with internal wall

This example, which was firstly proposed in [64], consists in a 90° curved 2D pipe conforming an elbow shape (Fig. 16). A zero-thickness wall is placed inside the curved pipe, generating two separated fluid ducts with space varying cross section area. Even though the zero-thickness wall could be alternatively modelled by duplicating the interface nodes, we represent it with a discontinuous level set function.

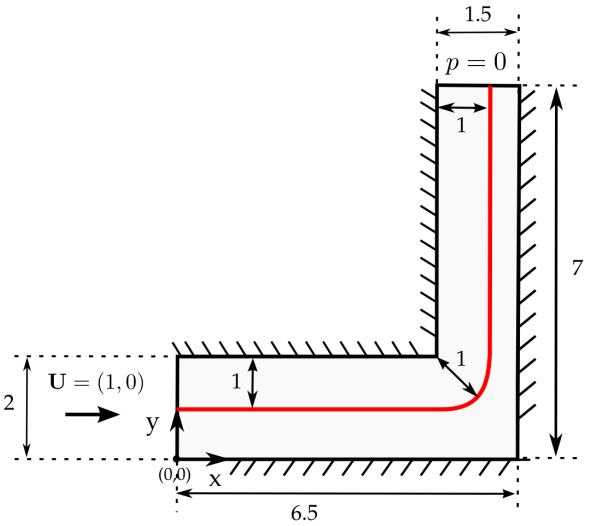

Figure 16 2D elbow with internal wall. Problem geometry (source[64]).

The previously described elbow geometry is solved using several mesh refinement levels and considering both a slip interface, as was done by the original authors in[64], as well as a no-slip one. The obtained solutions are compared with the ones obtained with a reference body fitted solver. Furthermore, we also evaluate the results with the literature and analytical values, which can be easily obtained from the mass conservation principle.

The fluid properties are selected to yield a unit *Re*. Considering the width of each one of the ducts as reference length and a constant inlet velocity u_x of 1m/s, the unit *Re* is achieved by setting ρ and μ to 1kg/m^3 and 1kg/ms. In all cases, the velocity is constrained to zero in the outer walls while the pressure is fixed to zero along the outlet edge. The BDF2 time scheme is used for the time discretization with a constant time time step equal to 10^{-2}s. The total simulation time is 1s, which is enough to reach a steady solution.

4.4.1 | Slip interface

For the sake of a fair comparison, the meshes employed in this case are set as similar as possible to the reference ones in[64]. Hence, we use four structured triangular grids (denoted as coarse, medium, fine and very fine) whose number of elements are collected in Table 9.

Considering that the reference solution assumes a pure slip behaviour in the intermediate wall, we set the slip length ϵ to 10^8m, which is a large enough value to yield a solution in the slip limit.

Table 9 2D elbow with internal wall. Number of elements for different refinement levels.

Mesh	Reference	Present work
Coarse	2400	2300
Medium	9600	8900
Fine	38400	36200
Very fine	153600	147000

Prior to any convergence assessment, we present the solution obtained with the medium refinement mesh in Fig. 17. As can be observed, the flow discontinuities arising from the introduction of the zero-thickness wall are perfectly captured by

the formulation. As a consequence, the wall contraction generates a pressure gradient in the right duct, which turns into an acceleration to preserve the inlet flow rate. On the contrary, the left duct pressure gradient is almost constant since there is no variation in the cross section. Hence, the minor differences between the left duct inlet and outlet pressure values are due to the local energy losses that occur when the flow changes its direction in the elbow.

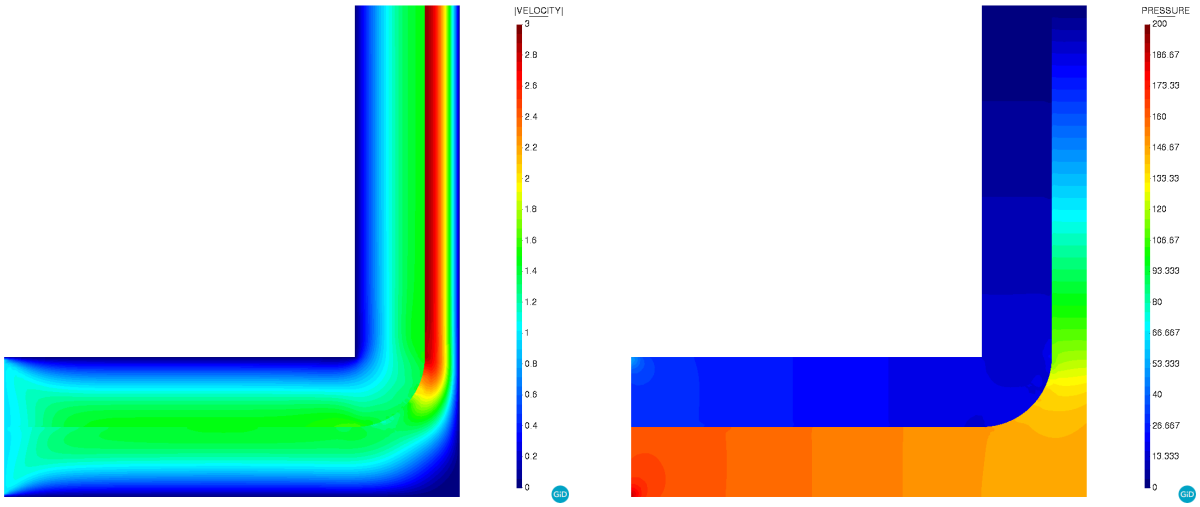

(a) Velocity modulus [m/s].

(b) Pressure [Pa].

Figure 17 2D elbow with internal wall (slip interface). Medium mesh solution.

Fig. 18 collects the current benchmark results assessment. On the one hand, Fig. 18a compares the obtained solution with a body fitted reference one as well as with the results reported in[47]. On the other hand, Fig. 18b depicts the convergence of the presented formulation. In both cases, the magnitude of reference is the y-component of the velocity along the outlet edge.

We observe a good correlation between all the solutions presented in Fig. 18a. Furthermore, it is also due mentioning that only minor differences can be observed between the discontinuous embedded penalty-based formulation presented in[47] and the Nitsche-based one presented in this work. Such minor differences manifest in the values close to the wall, being the Nitsche-based formulation slightly more accurate than the penalty one. This is more noticeable in the right duct due to the higher fluid velocity.

We also note that the solution convergence to the reference values as the mesh is refined (Fig. 18b). This is more evident in the values close to the embedded wall (Table 10), which significantly improve upon refinement due to the inability of the Ausas FE space to properly capture the gradients in one of the intersection sides.

Finally, Table 10 compares the outlet maximum y-component velocity values with the analytical ones. According to[64], if we consider the flow as parabolic in both sides of the intermediate wall, it can be proven that the analytical maximum velocity is 1.5m/s in the left duct and 3m/s in the right one. Once again, the values converge to the expected solution as the mesh is refined.

4.4.2 | No-slip interface

In this section we modify the 2D elbow test case to consider a no-slip behaviour in the intermediate wall. Although the geometry is the same, in this case it makes sense to consider a parabolic inlet in both ducts in accordance to the no-slip constraints in the outer and intermediate walls. However, preliminary tests showed that one of the ducts flow rate is always influenced by the inlet intersection pattern due to the Ausas FE space constant interpolation that occurs in one of the split sides. For this reason, we modify the inlet function to consider not the entire left side of each duct but the 75% of their length, so to ensure that the intersection pattern never influences the total flow rate. Thus, the bottom duct inlet function reads

$$v_x(y) = y(-12.642y + 9.4812) \tag{21}$$

while the top one is

$$v_x(y) = -12.642y^2 + 41.0864y - 31.6049 \tag{22}$$

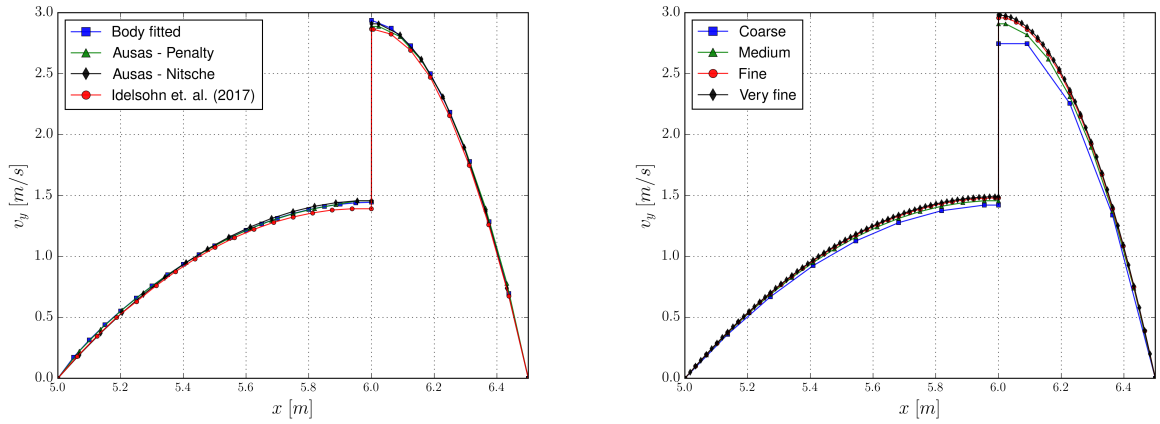

(a) Medium mesh comparison.

(b) Nitsche-based formulation convergence.

Figure 18 2D elbow with internal wall (slip interface). Outlet v_y [m/s].

Table 10 2D elbow with internal wall (slip interface). Outlet maximum velocity y-component for different refinement levels [m/s].

	$\|\mathbf{v_y}\|^{left}_{max}$	abs. err.	$\|\mathbf{v_y}\|^{right}_{max}$	abs. err.
Expected	1.5	-	3.0	-
Coarse	1.4213	0.0787	2.7459	0.2541
Medium	1.4569	0.0431	2.9089	0.0911
Fine	1.4805	0,0196	2.9574	0,0426
Very fine	1.4902	0,0098	2.9804	0,0196

Note that these parabolic functions preserve the inlet flow rates of the original benchmark case.

Taking into account the influence that the no-slip boundary condition has in the solution, we decided to use a new set of finer meshes to properly capture the expected parabolic solution. The new mesh sizes are related in Table 11.

Table 11 2D elbow with internal wall (no-slip interface). Element size for different refinement levels.

Mesh	Element size [m]
Body fitted	0.01
Embedded (coarse)	0.07
Embedded (medium)	0.0175
Embedded (fine)	0.01

Fig. 19 depicts the medium mesh embedded solution. As it can be observed, the imposition of the no-slip constraint in the intermediate wall yields the expected symmetric parabolic profile and pressure gradient in both ducts.

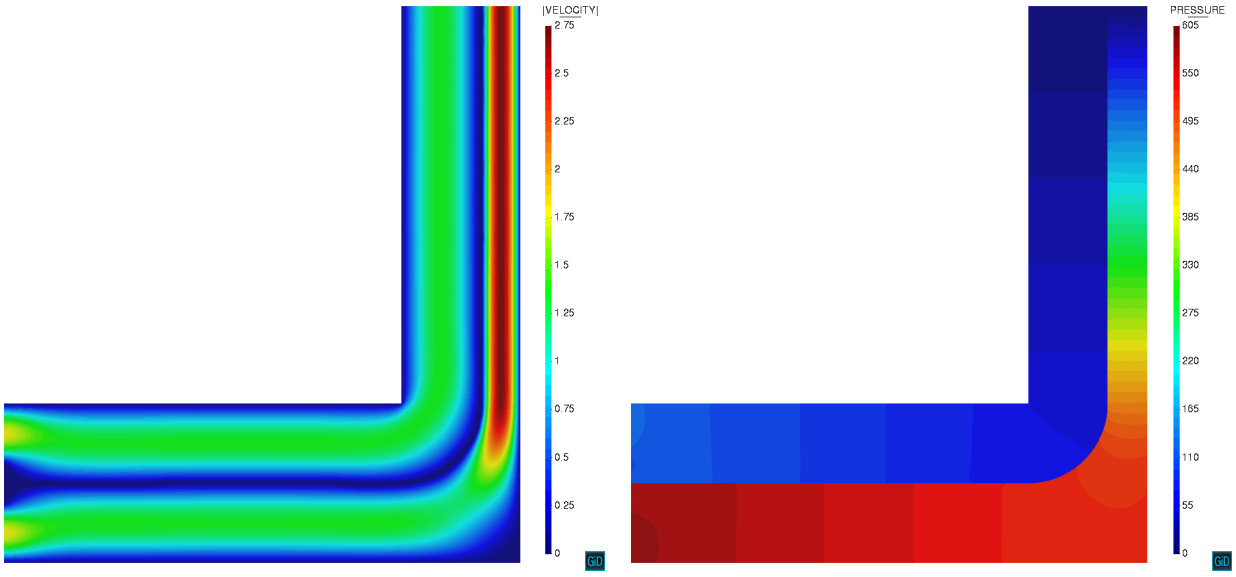

(a) Velocity modulus [m/s].

(b) Pressure [Pa].

Figure 19 2D elbow with internal wall (no-slip interface). Medium mesh solution.

Fig. 20 compares the the solution obtained with the three meshes with the reference body fitted solution. We note that the Nitsche embedded solution converges to the body fitted one as the mesh is refined. It is worth mentioning that the solutions with lower accuracy have a higher peak velocity value. This is explained by the inability of the Ausas FE space to properly capture the solution in the elements intersected by the no-slip intermediate wall. Considering that no velocity gradient can be captured in one side of these elements, the velocity becomes null (in a variational sense) over the entire element. As we mentioned before, this can be thought of as an extra kinematic constraint that weakly enforces the values in the embedded interface to be transferred to the nodes by the intersected edges. In the current zero velocity case, this turns into a sort of artificial shrinkage of the duct that requires the flow to accelerate in order to keep the inlet flow rate.

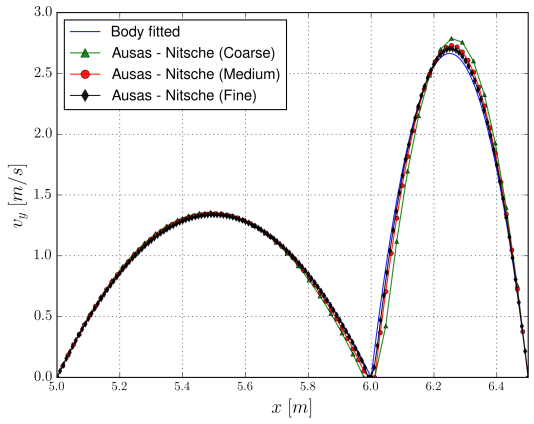

Figure 20 2D elbow with internal wall (no-slip interface). Outlet v_y [m/s].

Similarly to what we do for the slip case, Table 12 compares the reference analytical values, which can be easily obtained considering a parabolic flow and mass conservation, with the ones corresponding to the three refinement levels. Again, it can be checked that the no-slip solution converges to the reference one as the mesh is refined.

Table 12 2D elbow with internal wall (no-slip interface). Outlet maximum velocity y-component for different refinement levels [m/s].

	$\lvert\mathbf{v_y}\rvert_{max}^{left}$	abs. err.	$\lvert\mathbf{v_y}\rvert_{max}^{right}$	abs. err.
Expected	1.3332	-	2.6664	-
Coarse	1.3577	0.0245	2.7874	0.121
Medium	1.3492	0.016	2.7304	0.064
Fine	1.3370	0.0038	2.7011	0.0347

4.5 | 2D flow around thin-walled arch profile

This example is conceived to be a transition case between the academic examples we have presented so far and the final one in the next section. The geometry is a 20x100m rectangular channel in which a 4m chord and 1m height arch geometry is embedded. The embedded arch geometry is thought to be reasonably similar to the cross-section of a real 3D thin-walled structure (e.g. a sail or lightweight roof cover). Assuming that the bottom left corner of the channel is placed in the (0,0)m coordinates, the arch can be created from the three points (-2,-0.5), (0,0.5) and (2,-0.5)m. These geometry settings yield a 5% blockage coefficient. The material properties are set such that the *Re* is 10^5. Taking the height of the arch as reference length for the *Re* calculation, this can be achieved by setting ρ and μ to 1kg/m^3 and 1e-5kg/ms.

The BCs are rather simple. A constant inlet velocity of 1m/s is imposed in the left edge of the channel while the pressure is fixed to 0Pa in the right one. A symmetry BC (zero normal velocity and free tangential velocity) is imposed in the top and bottom edges. Concerning the embedded body BC, we consider two scenarios. The first one is the ideal slip case, in which ϵ is set to 1e8m. Secondly, we set ϵ to 1e-3m which is of the same order of magnitude as the theoretical boundary layer thickness corresponding to the current *Re*.

Both the body fitted and the embedded meshes have around 320k linear triangular elements. We note that in the body fitted case the boundary edges representing the arch geometry are duplicated in order to model the velocity and pressure discontinuities. Concerning the time discretization, we use the BDF2 scheme again. In all cases the time step is 0.05s.

4.5.1 | Slip interface

Fig. 21 presents the time evolution of the drag and lift forces. As it can be observed, both the body fitted and the embedded solutions reach a steady state solution with negligible drag force. Concerning the lift force, the embedded solution one is 1.60N while the body fitted reference one is 1.66N. Although the steady values are similar, we note that the embedded solution is more chaotic during the initial transient phase, and thus requires more time to approach the steady state.

Complementary, Figs. 22 and 23 compare the body fitted and embedded steady state solutions, which are in remarkably good agreement. It can be also observed that the steady solution presents a symmetric distribution, which explains the null horizontal drag component.

4.5.2 | No-slip interface

As we do for the slip interface case, we present in Fig. 24 the time evolution of the drag and lift forces. Taking into account that the no-slip solution is no longer steady, we complement this information with the histograms of such data series. The embedded

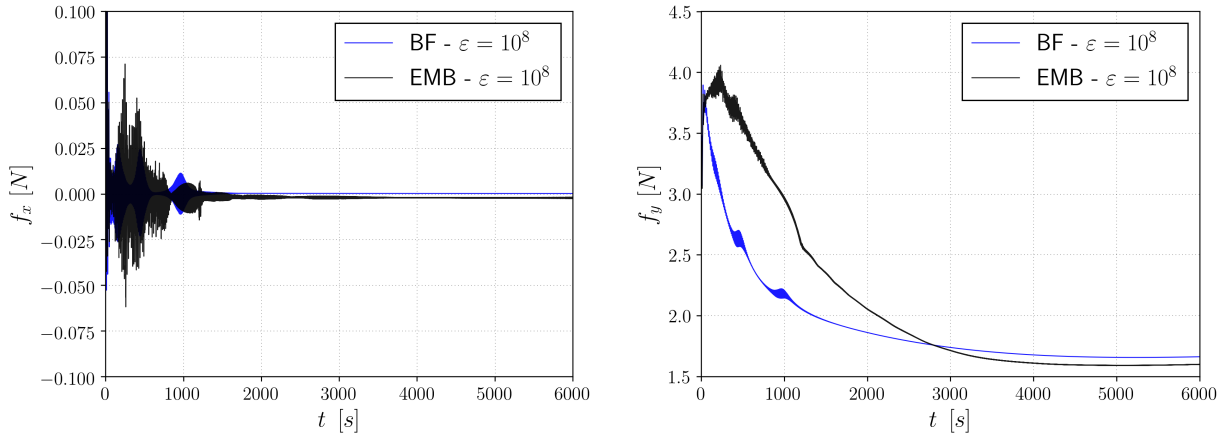

(a) Drag force [N].

(b) Lift force [N].

Figure 21 2D flow around thin-walled arch profile (slip interface). Drag and lift force time evolution.

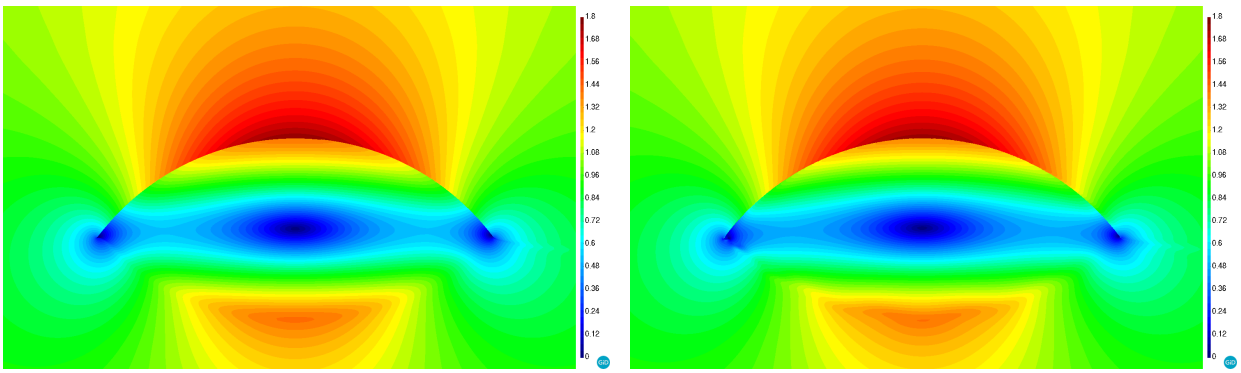

(a) Body fitted.

(b) Embedded.

Figure 22 2D flow around thin-walled arch profile (slip interface). Velocity modulus [m/s].

and body fitted drag force histograms are in very good agreement, being the average drag value around 0.2N (Fig. 24b). To what concerns the lift force, we observe that the embedded values are more disperse than the body fitted ones (Fig. 24d).

Fig. 25 presents two snapshots of the obtained embedded solution. We observe the presence of a stagnation point in the front end of the arch. Moreover, we also note the turbulent nature of the flow, which separates at the top part of the arch. After the separation point, whose location is approximately at one quarter of the total arch length, small vortexes appear alongside the solution discontinuity. In addition to these, a larger vortex appears in the trailing part of the arch. In the lower side of the arch, the flow presents a chaotic behaviour.

Last but not least, we would like to highlight the capability of the method to correctly impose not only the slip condition but also the no-slip one. We think that these results are crucial for the extension of the proposed technique to real engineering applications.

4.6 | 3D flow around a sailboat

The objective of this last example is to exploit the capabilities of the proposed formulation to efficiently solve a real engineering problem. Aiming to take advantage of the ability of the method to conveniently deal with membrane-like bodies, we choose a real sailboat geometry as final test case. Prior to any further discussion, it is due mentioning that no reference solution of any type is available for the problem at hand. Hence, we conceive this example as a proof-of-concept of one potential industrial application of the proposed technique.

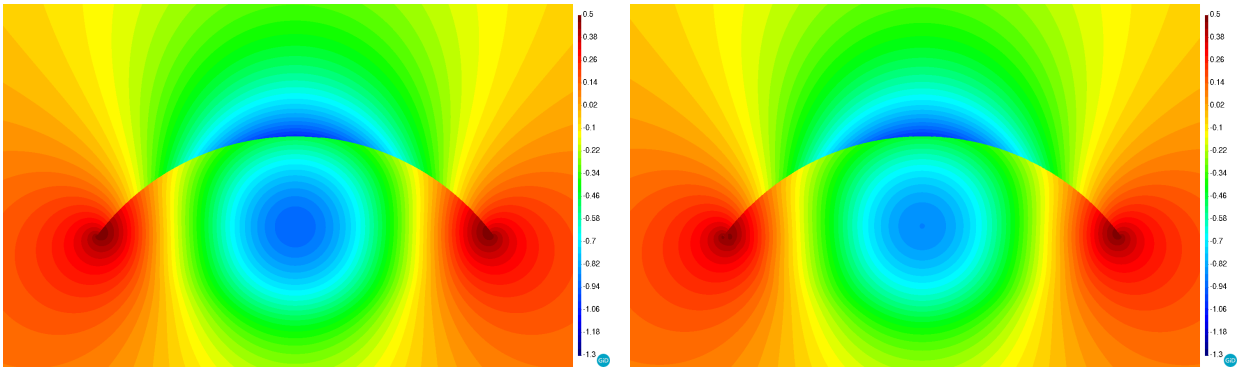

(a) Body fitted. **(b)** Embedded.

Figure 23 2D flow around thin-walled arch profile (slip interface). Pressure [Pa].

Figs. 28a and 29a depict the geometry of the sailboat, which has been provided by Juan Kouyoumdjian Naval Architects. The maximum length and beam of the hull are 18.3m and 5.75m while the mast height is around 27m. The mast axis is placed in the coordinates origin.

The computational domain is a 80m radius and 70m height cylinder centred in the (13.8,0,16.5)m coordinates (Fig. 26). The lateral surface of the cylinder is divided in two regions. The light green one is the outlet, which comprises one quarter of the cylinder skin, while the light pink one is the inlet.

The sailboat input geometry entities are separated in two sets according to their volume nature. On the one hand, we group those ones that conform bodies with well-defined internal volume (i.e. the hull and the mast), that is to say, those ones that can be straightforwardly represented using a body conforming discretization. On the other hand, we create a separate set containing all the surfaces that represent the sails.

By doing this we completely avoid the volume meshing of the thin-walled structures. It is known that generating a volume mesh from membrane-like bodies is a troublesome operation as it requires to duplicate the volumeless geometries to create a sort of zero volume body. Although this may seem a simple geometrical operation, it easily turns into a limitation since the polygonal representations of the duplicated surfaces tend to intersect each other when meshing the problem. Such complexity is completely bypassed by implicitly representing the mainsail as well as the headsails with a discontinuous distance function.

Once arrived to this point it is worth to spend some words on the level set calculation. Unlike the previous examples, in which the level set can be analytically determined, this example requires the use of a distance calculation algorithm. The basis, implementation details and treatment of corner cases of our choice can be found in[65]. Figs. 28 and 29 compare the input boat geometry to the computational one used in the resolution of the problem, which already includes the level set representation of the sails. As it can be observed, the embedded representation of the sails is in general terms very accurate. However, we note that the boundaries of the reconstructed geometry exhibit a “saw-toothed” pattern. This behaviour, which is also reported for a similar case in[47], is inherent to the level set method, which cannot represent the partial intersections that do not completely split the element in two parts.

The boundary conditions are rather simple. A slip BC is imposed in both the hull and the mast as well as in the top and bottom surfaces of the computational domain. The pressure is fixed to 0Pa in the outlet surface. In the inlet one a wind velocity of 15knots (7.72m/s) is imposed in the (1,0,1) direction, which is rotated 45° with respect to the alignment of the hull. With regard to the Navier-slip BC in the embedded sails, the ϵ is set to 1e-2m while the penalty constant γ is equal to 0.25. The problem is run for 20s using a time step Δt of 0.025s. The computational domain is meshed with 3.3M of linear tetrahedra. Fig. 27 shows a detail the volume mesh surrounding the hull and the mast.

Despite the lack of either analytical or reference results, the obtained velocity and pressure fields are convincing. As it can be observed in Fig. 30c, the proposed formulation is capable of representing the pressure discontinuity between the two sides of the embedded sails. A positive overpressure appears in the windward region of the sails (Fig. 30a) while a suction occurs in the leeward one (Fig. 30b). Such pressure jump generates the thrust of the sailboat.

Fig. 31 presents a set of velocity horizontal cross sections which depict the velocity discontinuities between the windward and leeward sides. It is also interesting to comment on the effect that the slip length has in the solution. This can be clearly noted in the front sail, specially in the plane y equal to 5 m cross section(Fig. 31b). Despite the separation that occurs in the front

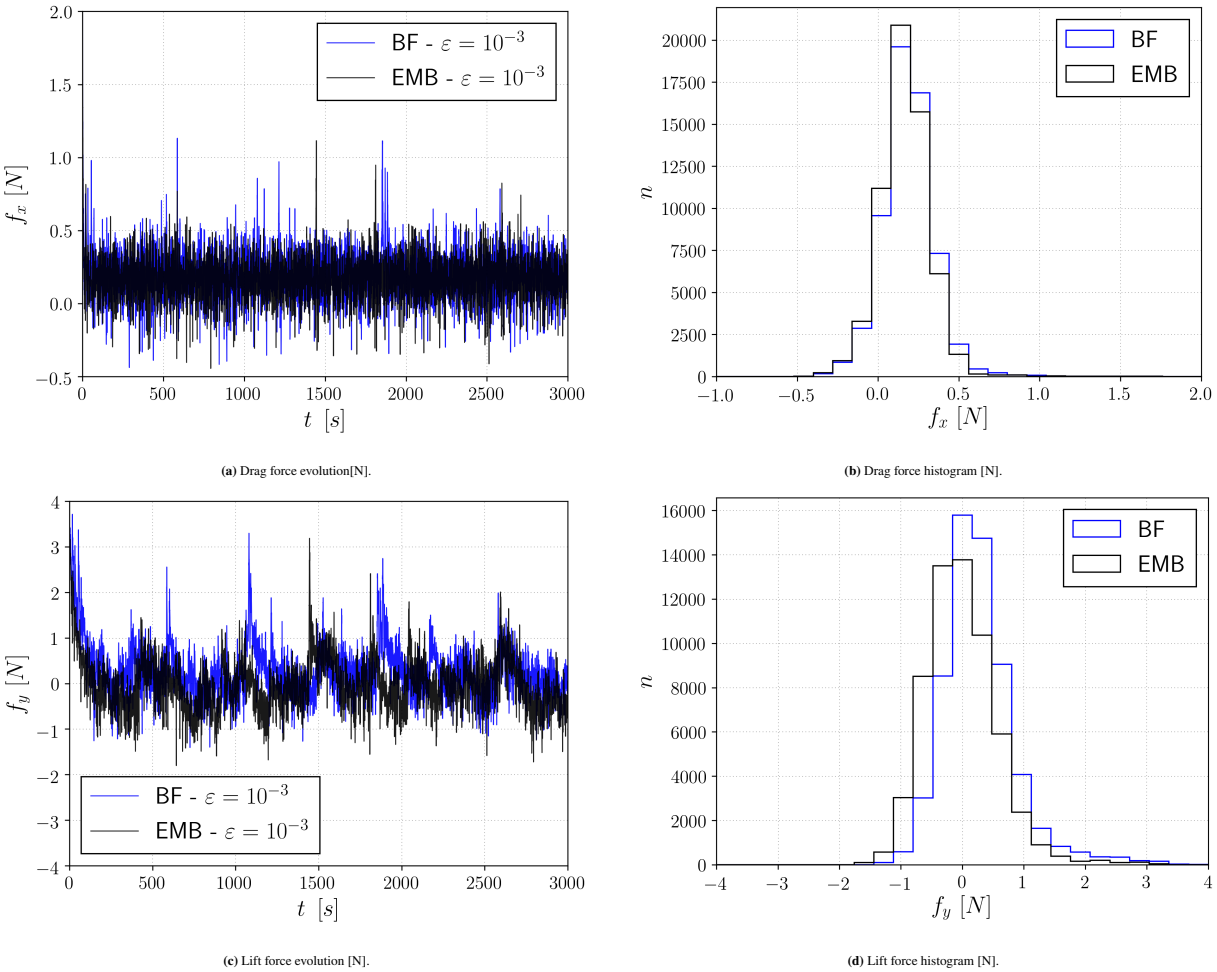

(a) Drag force evolution[N].

(b) Drag force histogram [N].

(c) Lift force evolution [N].

(d) Lift force histogram [N].

Figure 24 2D flow around thin-walled arch profile (no-slip interface). Drag and lift force.

edge of the sail, the velocity is neither null (no-slip condition) nor maximum (slip condition) in the sail surface. Instead, the velocity field behaves as a sort of wall law, which is expected to be the nature of the Navier-slip BC. Despite the lack of a more rigorous study about the effect that alternative ε value could have in the solution, we believe that these preliminary experiments are promising from the industrial application perspective.

5 | CONCLUSION

This work presents a novel embedded formulation for the weak imposition of the Navier-slip BC in viscous incompressible Navier-Stokes flows. We particularly focus on the nature of the embedded bodies to enable the simulation of any type of geometries. Hence, our proposal is valid not only for volumetric bodies but also for membrane-like ones that feature no internal volume.

The new formulation relies on the use of the Ausas FE space in combination with a Nitsche-based imposition of the Navier-slip BC. Provided a discontinuous level set function representing the immersed objects, the Ausas FE space is able to capture both velocity and pressure discontinuities inside the intersected elements. On top of that, the Navier-slip BC that is enforced in the level set intersections makes possible the imposition of any wall behaviour from the slip to the no-slip limits.

The proposed technique is purely local, meaning that it neither requires a special treatment of the blending elements nor the introduction of extra degrees of freedom. While the former becomes relevant when working with distributed memory environments (MPI), the latter avoids the need of reconstructing the discrete system matrix graph each time the level set is updated , something that arguably would impede the practical application of the method to large FSI problems.

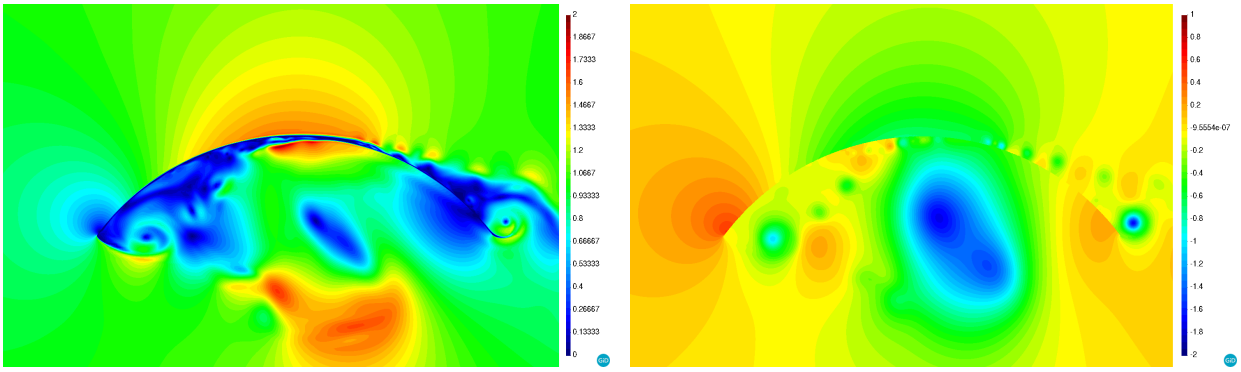

(a) Velocity modulus [m/s].

(b) Pressure [Pa].

Figure 25 2D flow around thin-walled arch profile (no-slip interface). Embedded solution snapshots.

We assess convergence and accuracy by solving several examples, which consider different values of the slip length that range from the slip to the no-slip limits. For ϵ values close to the slip limit, we observe that both velocity and pressure convergence rates are $O(h^{3/2})$, which is in accordance with the interpolation properties of the Ausas FE space[47,48]. However, the convergence rates deteriorate to $O(h)$ when the slip length approaches the no-slip limit. Such degradation can be perfectly expected due to the inability of the Ausas FE space to properly represent the gradients within the intersected elements. Nonetheless, we note that the wall shear effects are roughly recovered upon mesh refinement as the "thickness" of the constant solution (i.e. zero gradient) region is reduced.

Complementary, we also prove the ability of the extra pseudo-compressibility term in the mass conservation equation to keep the pressure bounded by solving one example involving isolated fluid cavities with no Neumann BC. We highlight that this is crucial for the effective application of the method to ill-conditioned level set functions coming from "dirty" input geometries.

The experimental campaign is completed with two examples involving high *Re* turbulent flows. While the first involves a simple 2D geometry, the second is a feasible industrial application. The utility of the method to completely get rid of the pre-processing difficulties that arise when trying to create a volume mesh from a thin-walled structure is evinced in this last example. In this context, the embedded viscous Navier-slip approach represents a reasonable alternative to the more expensive boundary layer mesh and no-slip BC combination.

Finally, it is interesting to point out the further enhancements and future work lines. The first one is to couple the proposed methodology with an structural mechanics solver to build an FSI framework for the analysis of highly flexible membrane and shell structures[50]. Another interesting application is the modelling of the fluid flow around thin biological tissues[3] or cardiac valves[32,66]. There is also room for theoretical advances. In this regard we want to explore the use of a discontinuous edge-based level set function which would help to handle some of the partial element intersection issues we report in the sailboat example.

ACKNOWLEDGEMENTS

The research was partly supported by the International Graduate School of Science and Engineering (IGSSE) through the project ATMOPACE and the European Comission (EC) through the project ExaQUte (H2020-FETHPC-2016-2017-800898). The authors also acknowledge financial support from the Spanish Ministry of Economy and Competitiveness, through the "Severo Ochoa Programme for Centres of Excellence in R&D" (CEX2018-000797-S). Dr. Larese gratefully acknowledges the support of the Italian ministry for her Rita Levi Montalcini fellowship (Programma per Giovani Ricercatori "Rita Levi Montalcini" - bando 2016) as well as the support of INDAM.

Finally, the authors also thank Juan Kouyoumdjian Naval Architects for providing the CAD models required to set up the 3D sailboat example.

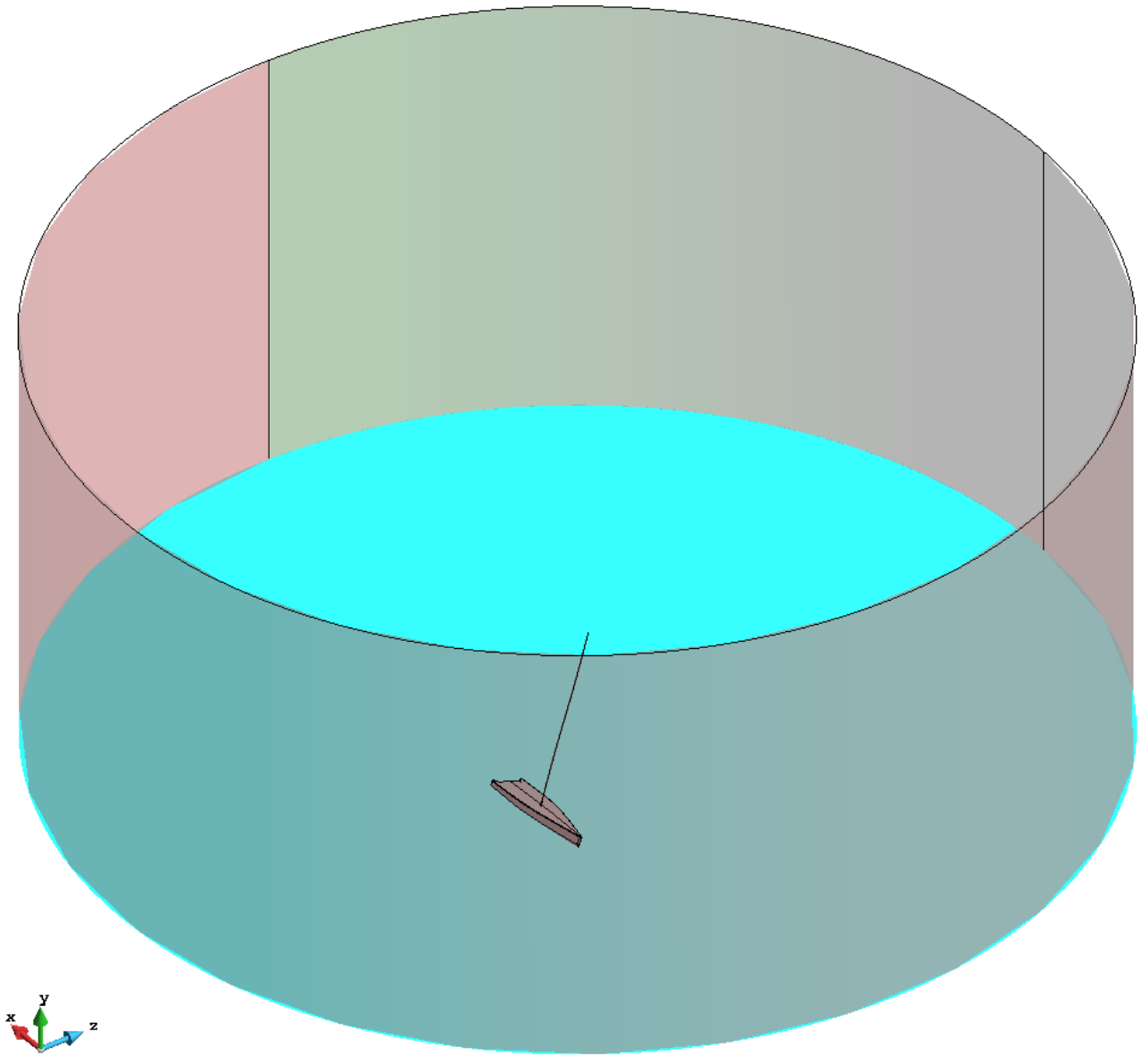

Figure 26 3D flow around a sailboat. Computational domain.

DATA AVAILABILITY STATEMENT

The datasets in the current study are available from the corresponding author on reasonable request. The code used to generate the datasets is available in the Kratos Multiphysics repository.

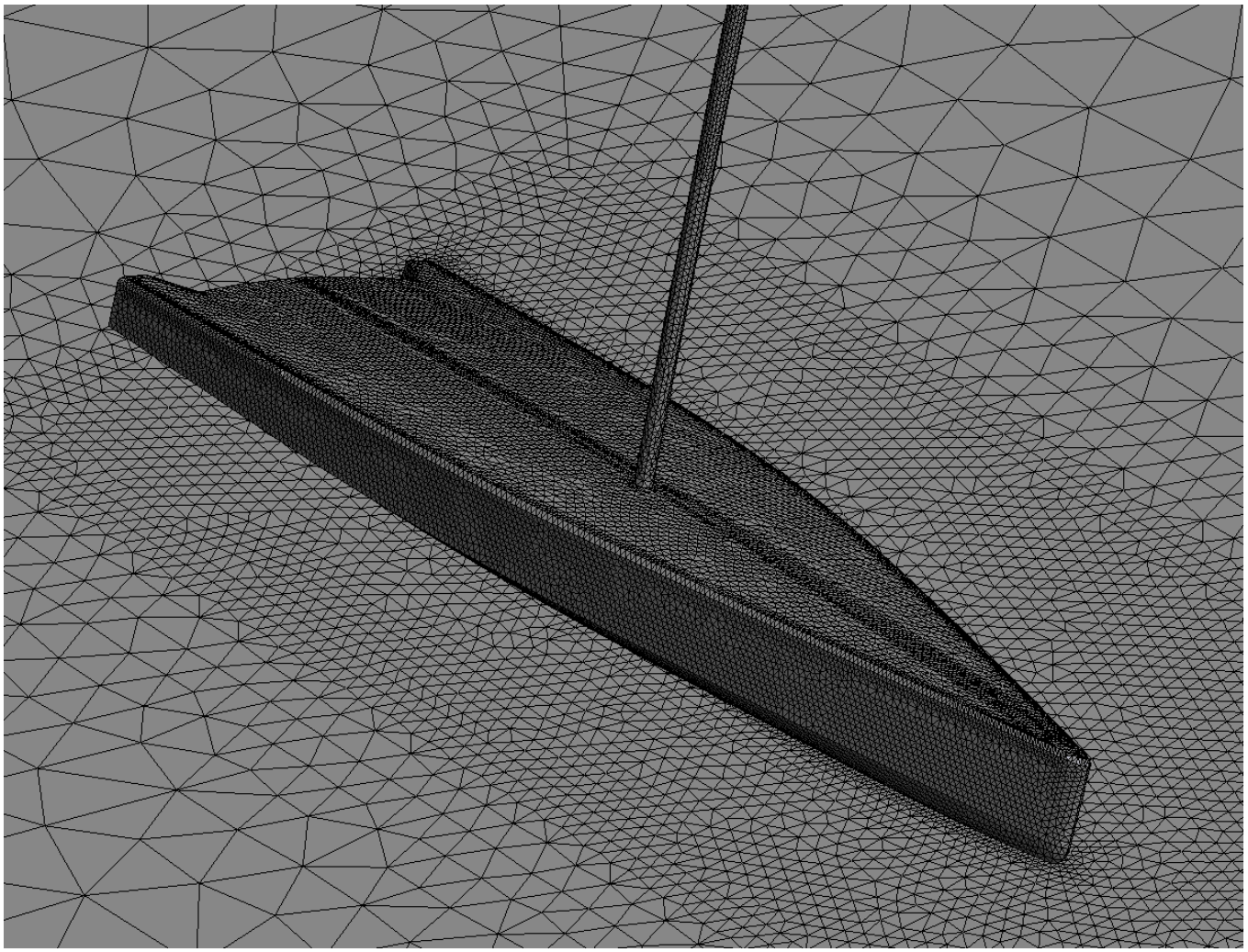

Figure 27 3D flow around a sailboat. Hull and mast mesh detail.

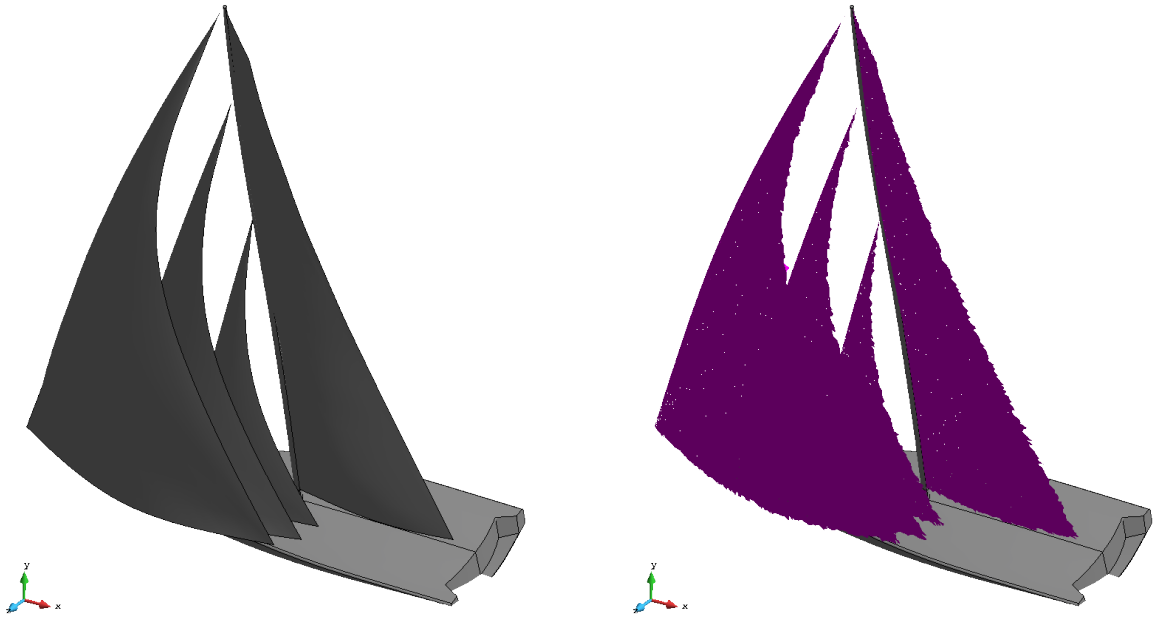

(a) Original geometry. **(b)** Computational model.

Figure 28 3D flow around a sailboat. Sailboat top-side view.

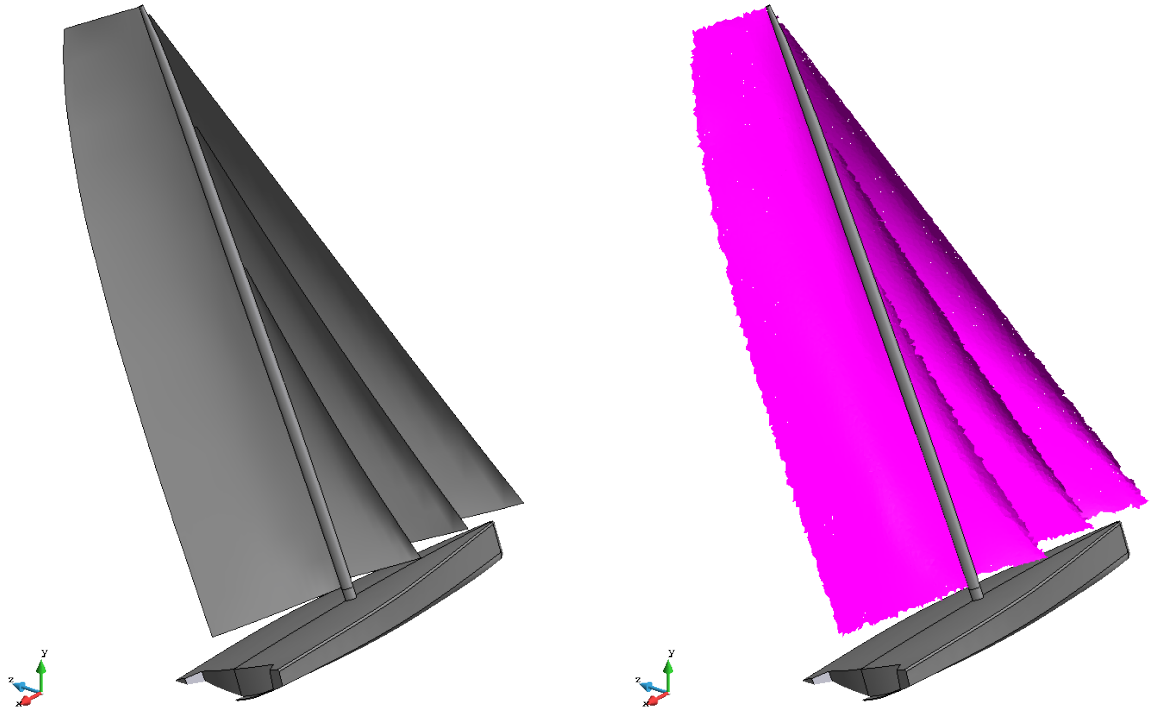

(a) Original geometry **(b)** Computational model.

Figure 29 3D flow around a sailboat. Sailboat top-rear view.

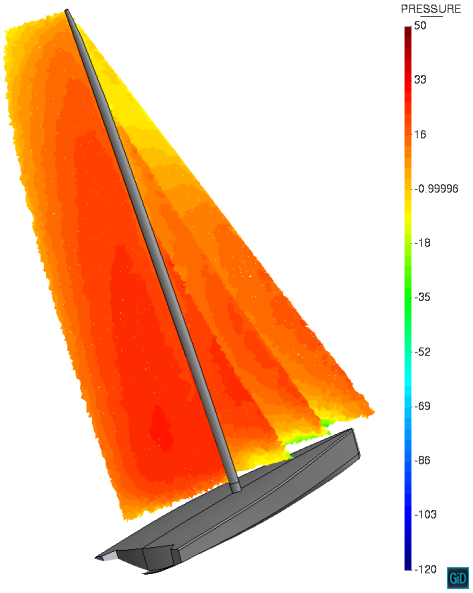

(a) Boat detail (windward).

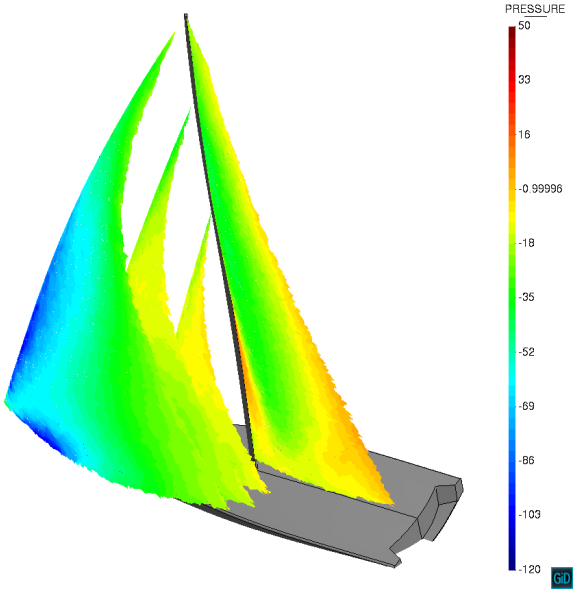

(b) Boat detail (leeward).

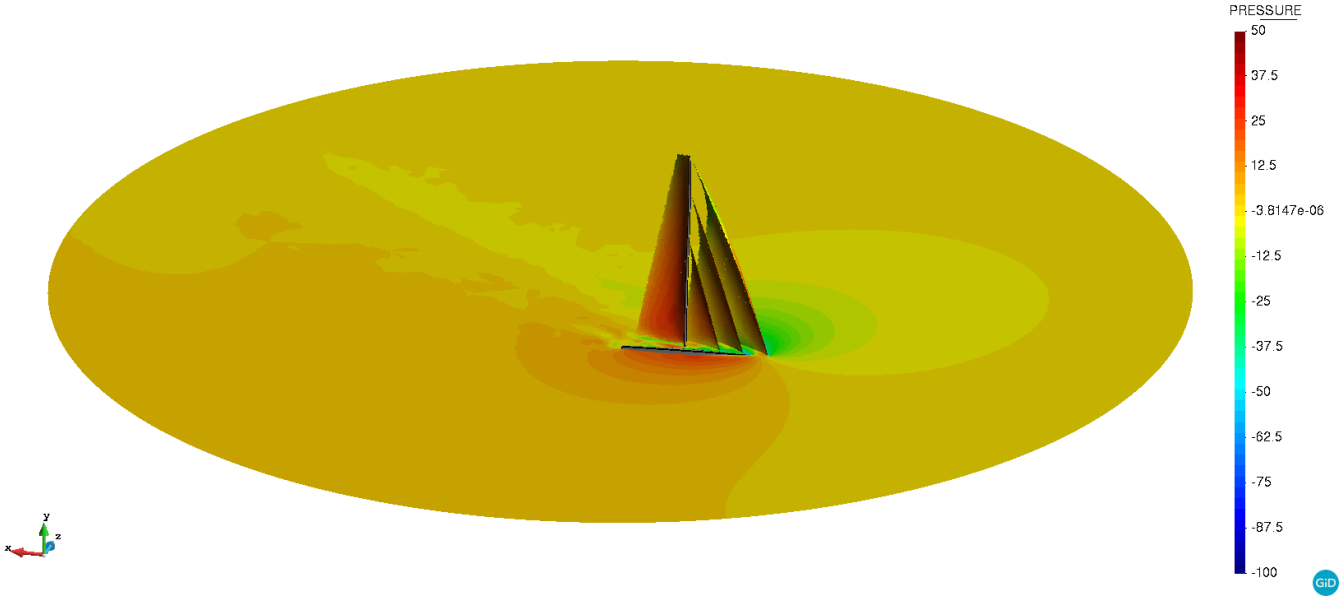

(c) Computational domain cross section.

Figure 30 3D flow around a sailboat. Pressure field.

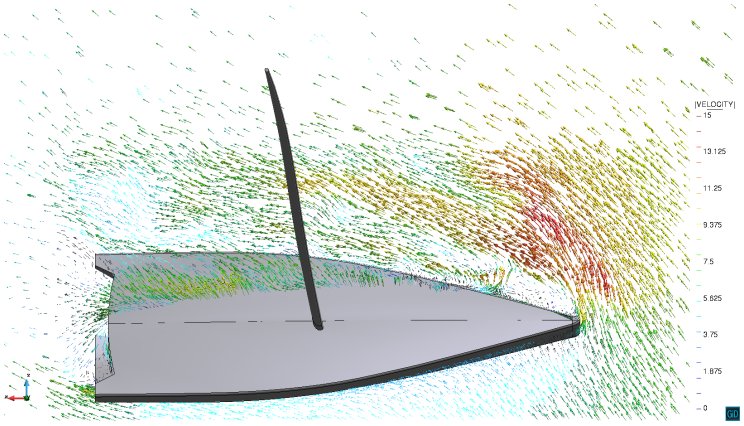

(a) Cross section at height 1m.

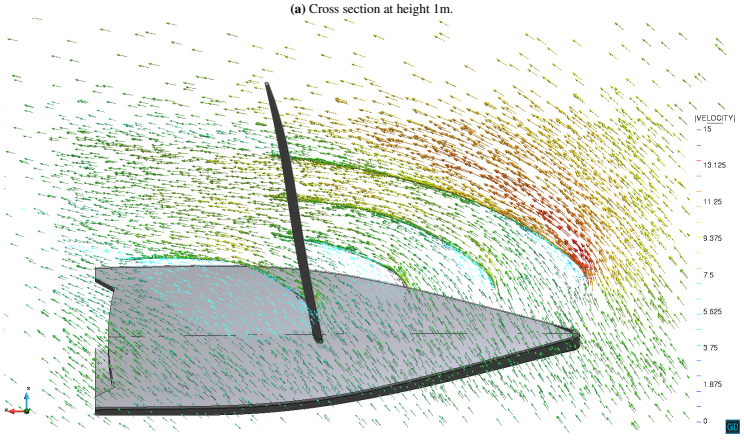

(b) Cross section at height 5m.

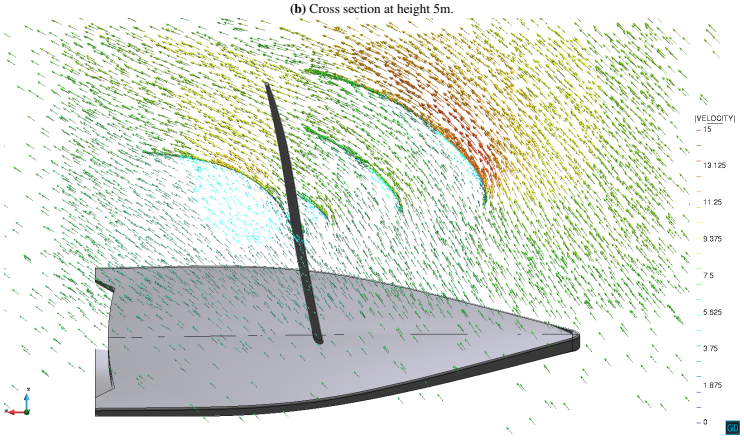

(c) Cross section at height 12.5m.

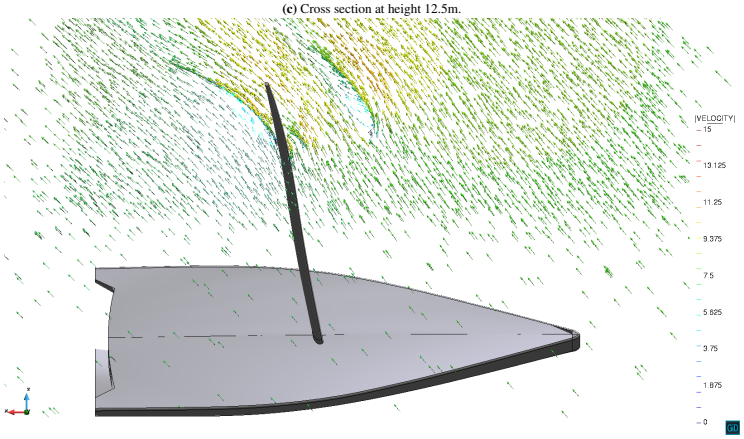

(d) Cross section at height 20m.

Figure 31 3D flow around a sailboat. Velocity field.

References

1. Scotta R, Lazzari M, Stecca E, Cotela J, Rossi R. Numerical wind tunnel for aerodynamic and aeroelastic characterization of bridge deck sections. *Computers & Structures* 2016; 167: 96 - 114. doi: 10.1016/j.compstruc.2016.01.012

2. Soudah E, Rudenick P, Bordone M, et al. Validation of numerical flow simulations against in vitro phantom measurements in different type B aortic dissection scenarios. *Computer Methods in Biomechanics and Biomedical Engineering* 2015; 18(8): 805-815. PMID: 24156535doi: 10.1080/10255842.2013.847095

3. Zorrilla R, Soudah E, Rossi R. Computational modeling of the fluid flow in type B aortic dissection using a modified finite element embedded formulation. *Biomechanics and Modeling in Mechanobiology* 2020. doi: 10.1007/s10237-020-01291-x

4. Versteeg HK, Malalasekera W. *An introduction to computational fluid dynamics: the finite volume method*. Pearson education . 2007.

5. Kim J, Kim D, Choi H. An Immersed-Boundary Finite-Volume Method for Simulations of Flow in Complex Geometries. *Journal of Computational Physics* 2001; 171(1): 132 - 150. doi: https://doi.org/10.1006/jcph.2001.6778

6. Oñate E, Franci A, Carbonell JM. Lagrangian formulation for finite element analysis of quasi-incompressible fluids with reduced mass losses. *International Journal for Numerical Methods in Fluids* 2014; 74(10): 699-731. doi: 10.1002/fld.3870

7. Donea J, Huerta A, Ponthot JP, Rodríguez-Ferran A. *Arbitrary Lagrangian–Eulerian Methods*ch. 14; American Cancer Society . 2004

8. S.Osher , Fedkiw R. *Level Set Methods and Dynamic Implicit Surfaces*. 153 of *Applied Mathematical Siences*. Springer-Verlag New York. 1 ed. 2003.

9. Hirt C, Amsden A, Cook J. An arbitrary Lagrangian-Eulerian computing method for all flow speeds. *Journal of Computational Physics* 1974; 14(3): 227-253. doi: 10.1016/0021-9991(74)90051-5

10. Bertrand F, Tanguy P, Thibault F. A three-dimensional fictitious domain method for incompressible fluid flow problems. *Int. J. Num. Meth. Fluids* 1997; 25(6): 719-736. doi: 10.1002/(SICI)1097-0363(19970930)25:6<719::AID-FLD585>3.0.CO;2-K

11. Mittal R, Dong H, Bozkurttas M, Najjar F, Vargas A, Loebbecke vA. A versatile sharp interface immersed boundary method for incompressible flows with complex boundaries. *Journal of Computational Physics* 2008; 227(10): 4825 - 4852. doi: 10.1016/j.jcp.2008.01.028

12. Zhao H, Freund JB, Moser RD. A fixed-mesh method for incompressible flow–structure systems with finite solid deformations. *Journal of Computational Physics* 2008; 227(6): 3114 - 3140. doi: 10.1016/j.jcp.2007.11.019

13. Casquero H, Zhang YJ, Bona-Casas C, Dalcin L, Gomez H. Non-body-fitted fluid–structure interaction: Divergence-conforming B-splines, fully-implicit dynamics, and variational formulation. *Journal of Computational Physics* 2018; 374: 625 - 653. doi: 10.1016/j.jcp.2018.07.020

14. Löhner R, Cebral J, Camelli F, et al. Adaptive embedded and immersed unstructured grid techniques. *Comput. Methods Appl. Mech. Engrg.* 2008; 197(25): 2173-2197. doi: 10.1016/j.cma.2007.09.010

15. Coll A. *Robust volume mesh generation for non-watertigh geometries*. PhD thesis. Universitat Politècnica de Catalunya, Pl. Eusebi Güell, 6, 08034 Barcelona; 2014.

16. Allaire G, Dapogny C, Frey P. A mesh evolution algorithm based on the level set method for geometry and topology optimization. *Structural and Multidisciplinary Optimization* 2013; 48(4): 711–715. doi: 10.1007/s00158-013-0929-2

17. Frey P, Alauzet F. Anisotropic mesh adaptation for CFD computations. *Computer Methods in Applied Mechanics and Engineering* 2005; 194(48): 5068 - 5082. doi: 10.1016/j.cma.2004.11.025

18. Benard P, Balarac G, Moureau V, Dobrzynski C, Lartigue G, D'Angelo Y. Mesh adaptation for large-eddy simulations in complex geometries. *International Journal for Numerical Methods in Fluids* 2015; 81(12): 719-740. doi: 10.1002/fld.4204

19. Peskin C. Numerical analysis of blood flow in the heart. *Journal of Computational Physics* 1977; 25(3): 220 - 252. doi: 10.1016/0021-9991(77)90100-0

20. Peskin C. The immersed boundary method. *Acta Numerica* 2002; 112: 479 - 517. doi: 10.1017/S0962492902000077

21. Foucard L, Vernerey F. An X-FEM-based numerical–asymptotic expansion for simulating a Stokes flow near a sharp corner. *International Journal for Numerical Methods in Engineering* 2015; 102(2): 79-98. doi: 10.1002/nme.4746

22. Sawada T, Tezuka A. LLM and X-FEM based interface modeling of fluid–thin structure interactions on a non-interface-fitted mesh. *Computational Mechanics* 2011; 48(3): 319–332. doi: 10.1007/s00466-011-0600-y

23. Alauzet F, Fabrèges B, Fernández MA, Landajuela M. Nitsche-XFEM for the coupling of an incompressible fluid with immersed thin-walled structures. *Computer Methods in Applied Mechanics and Engineering* 2016; 301: 300 - 335. doi: 10.1016/j.cma.2015.12.015

24. Schott B, Shahmiri S, Kruse R, Wall W. A stabilized Nitsche-type extended embedding mesh approach for 3D low- and high-Reynolds-number flows. *International Journal for Numerical Methods in Fluids* 2016; 82(6): 289-315. doi: 10.1002/fld.4218

25. Burman E, Hansbo P. Fictitious domain finite element methods using cut elements: I. A stabilized Lagrange multiplier method. *Computer Methods in Applied Mechanics and Engineering* 2010; 199(41): 2680-2686. doi: 10.1016/j.cma.2010.05.011

26. Burman E, Hansbo P. Fictitious domain finite element methods using cut elements: II. A stabilized Nitsche method. *Applied Numerical Mathematics* 2012; 62(4): 328-341. doi: 10.1016/j.apnum.2011.01.008

27. Burman, Erik , Hansbo, Peter . Fictitious domain methods using cut elements: III. A stabilized Nitsche method for Stokes´ problem. *ESAIM: M2AN* 2014; 48(3): 859-874. doi: 10.1051/m2an/2013123

28. Massing A, Larson M, Logg A, Rognes M. A Stabilized Nitsche Fictitious Domain Method for the Stokes Problem. *Journal of Scientific Computing* 2014; 61(3): 604-628. doi: 10.1007/s10915-014-9838-9

29. Burman E, Claus S, Hansbo P, Larson MG, Massing A. CutFEM: Discretizing geometry and partial differential equations. *International Journal for Numerical Methods in Engineering* 2015; 104(7): 472-501. doi: 10.1002/nme.4823

30. Main A, Scovazzi G. The shifted boundary method for embedded domain computations. Part I: Poisson and Stokes problems. *Journal of Computational Physics* 2018; 372: 972 - 995. doi: 10.1016/j.jcp.2017.10.026

31. Main A, Scovazzi G. The shifted boundary method for embedded domain computations. Part II: Linear advection–diffusion and incompressible Navier–Stokes equations. *Journal of Computational Physics* 2018; 372: 996 - 1026. doi: 10.1016/j.jcp.2018.01.023

32. Kamensky D, Hsu MC, Schillinger D, et al. An immersogeometric variational framework for fluid–structure interaction: Application to bioprosthetic heart valves. *Computer Methods in Applied Mechanics and Engineering* 2015; 284: 1005 - 1053. doi: 10.1016/j.cma.2014.10.040

33. Xu F, Kamensky D, Varduhn V, et al. *An Immersogeometric Method for the Simulation of Turbulent Flow Around Complex Geometries*: 111–125; Cham: Springer International Publishing . 2016

34. Babuška I. The finite element method with penalty. *Mathematics of computation* 1973; 27(122): 221–228. doi: 10.1090/S0025-5718-1973-0351118-5

35. Glowinski R, Pan TW, Periaux J. A Lagrange multiplier/fictitious domain method for the Dirichlet problem — Generalization to some flow problems. *Japan Journal of Industrial and Applied Mathematics* 1995; 12(1): 87. doi: 10.1007/BF03167383

36. Glowinski R, Pan T, Périaux J. Distributed Lagrange multiplier methods for incompressible viscous flow around moving rigid bodies. *Computer Methods in Applied Mechanics and Engineering* 1998; 151(1): 181 - 194. Containing papers presented at the Symposium on Advances in Computational Mechanicsdoi: 10.1016/S0045-7825(97)00116-3

37. Nitsche J. Über ein Variationsprinzip zur Lösung von Dirichlet-Problemen bei Verwendung von Teilräumen, die keinen Randbedingungen unterworfen sind. *Abhandlungen aus dem Mathematischen Seminar der Universität Hamburg* 1971; 36(1): 9-15. doi: 10.1007/BF02995904

38. Hansbo A, Hansbo P. An unfitted finite element method, based on Nitsche's method, for elliptic interface problems. *Computer Methods in Applied Mechanics and Engineering* 2002; 191(47): 5537-5552. doi: https://doi.org/10.1016/S0045-7825(02)00524-8

39. Hansbo P. Nitsche's method for interface problems in computa-tional mechanics. *GAMM-Mitteilungen* 2005; 28(2): 183-206. doi: https://doi.org/10.1002/gamm.201490018

40. Juntunen M, Stenberg R. Nitsche's method for general boundary conditions. *Mathematics of Computation* 2009; 78: 1353-1374. doi: 10.1090/S0025-5718-08-02183-2

41. Codina R, Baiges J. Approximate imposition of boundary conditions in immersed boundary methods. *Int. J. Numer. Meth. Engng.* 2009; 80: 1379-1405. doi: 10.1002/nme.2662

42. Massing A, Schott B, Wall W. A stabilized Nitsche cut finite element method for the Oseen problem. *Comput. Methods Appl. Mech. Engrg.* 2018; 328: 262-300. doi: 10.1016/j.cma.2017.09.003

43. Urquiza J, Garon A, Farinas MI. Weak imposition of the slip boundary condition on curved boundaries for Stokes flow. *Journal of Computational Physics* 2014; 256: 748-767. doi: 10.1016/j.jcp.2013.08.045

44. Winter M, Schott B, Massing A, Wall W. A Nitsche cut finite element method for the Oseen problem with general Navier boundary conditions. *Comput. Methods Appl. Mech. Engrg.* 2018; 330: 220-252. doi: 10.1016/j.cma.2017.10.023

45. Peskin C. Flow patterns around heart valves: A numerical method. *Journal of Computational Physics* 1972; 10(2): 252 - 271. doi: 10.1016/0021-9991(72)90065-4

46. Peskin C, McQueen D. A three-dimensional computational method for blood flow in the heart I. Immersed elastic fibers in a viscous incompressible fluid. *Journal of Computational Physics* 1989; 81(2): 372 - 405. doi: 10.1016/0021-9991(89)90213-1

47. Zorrilla R, Larese A, Rossi R. A modified Finite Element formulation for the imposition of the slip boundary condition over embedded volumeless geometries. *Computer Methods in Applied Mechanics and Engineering* 2019; 353: 123 - 157. doi: 10.1016/j.cma.2019.05.007

48. Ausas R, Sousa F, Buscaglia G. An improved finite element space for discontinuous pressures. *Comput. Methods Appl. Mech. Engrg.* 2010; 199: 1019-1031. doi: 10.1016/j.cma.2009.11.011

49. Baiges J, Codina R. The fixed-mesh ALE approach applied to solid mechanics and fluid–structure interaction problems. *International Journal for Numerical Methods in Engineering* 2010; 81(12): 1529-1557. doi: 10.1002/nme.2740

50. Zorrilla R, Rossi R, Wüchner R, Oñate E. An embedded Finite Element framework for the resolution of strongly coupled Fluid–Structure Interaction problems. Application to volumetric and membrane-like structures. *Computer Methods in Applied Mechanics and Engineering* 2020; 368: 113179. doi: 10.1016/j.cma.2020.113179

51. Dadvand P, Rossi R, Oñate E. An Object-oriented Environment for Developing Finite Element Codes for Multi-disciplinary Applications. *Archives of Computational Methods in Engineering* 2010; 17(3): 253–297. doi: 10.1007/s11831-010-9045-2

52. Dadvand P, Rossi R, Gil M, et al. Migration of a generic multi-physics framework to HPC environments. *Computers & Fluids* 2013; 80: 301 - 309. doi: 10.1016/j.compfluid.2012.02.004

53. Hughes T, Franca L, Balestra M. A new finite element formulation for computational fluid dynamics: V. Circumventing the babuška-brezzi condition: a stable Petrov-Galerkin formulation of the stokes problem accommodating equal-order interpolations. *Computer Methods in Applied Mechanics and Engineering* 1986; 59(1): 85 - 99. doi: 10.1016/0045-7825(86)90025-3

54. Tezduyar T, Mittal S, Ray S, Shih R. Incompressible flow computations with stabilized bilinear and linear equal-order-interpolation velocity-pressure elements. *Comput. Methods Appl. Mech. Engrg.* 1992; 95(2): 221-242. doi: 10.1016/0045-7825(92)90141-6

55. Cotela J, Rossi R, Oñate E. A FIC-based stabilized finite element formulation for turbulent flows. *Comput. Methods Appl. Mech. Engrg.* 2017; 315: 607 - 631. doi: 10.1016/j.cma.2016.11.020

56. Hughes T. Multiscale phenomena: Green's function, the dirichlet to Neumann formulation, subgrid scale models, bubbles and the origins of stabilized formulations. *Comput. Methods Appl. Mech. Engrg.* 1995; 127(1): 387-401. doi: 10.1016/0045-7825(95)00844-9

57. Hughes T, Feijóo G, Mazzei L, Quincy J. The variational multiscale method—a paradigm for computational mechanics. *Comput. Methods Appl. Mech. Engrg.* 1998; 166(1): 3-24. Advances in Stabilized Methods in Computational Mechanicsdoi: 10.1016/S0045-7825(98)00079-6

58. Codina R. Stabilized finite element approximation of transient incompressible flows using orthogonal subscales. *Computer Methods in Applied Mechanics and Engineering* 2002; 191(39): 4295 - 4321. doi: 10.1016/S0045-7825(02)00337-7

59. Codina R. A stabilized finite element method for generalized stationary incompressible flows. *Comput. Methods Appl. Mech. Engrg.* 2001; 190(20): 2681-2706. doi: 10.1016/S0045-7825(00)00260-7

60. Codina R, Principe J, Guasch O, Badia S. Time dependent subscales in the stabilized finite element approximation of incompressible flow problems. *Computer Methods in Applied Mechanics and Engineering* 2007; 196(21): 2413 - 2430. doi: 10.1016/j.cma.2007.01.002

61. Meurer A, Smith C, Paprocki M, et al. SymPy: symbolic computing in Python. *PeerJ Computer Science* 2017; 3: e103. doi: 10.7717/peerj-cs.103

62. Ausas R, Sousa F, Idelsohn S. A statically condensable enrichment for pressure discontinuities in two-phase flows. *Mecánica Computacional* 2011; 30(4): 175-191.

63. Davari M, Rossi R, Dadvand P. Three embedded techniques for finite element heat flow problem with embedded discontinuities. *Comput. Mech.* 2017; 59: 1003-1030. doi: 10.1007/s00466-017-1382-7

64. Idelsohn S, Gimenez J, Nigro N. Multifluid flows with weak and strong discontinuous interfaces using an elemental enriched space. *International Journal for Numerical Methods in Fluids* 2018; 86(12): 750-769. doi: 10.1002/fld.4477

65. Baumgärtner D, Wolf J, Rossi R, Dadvand P, Wüchner R. A robust algorithm for implicit description of immersed geometries within a background mesh. *Advanced Modeling and Simulation in Engineering Sciences* 2018; 5(1): 21. doi: 10.1186/s40323-018-0113-8

66. Hsu MC, Kamensky D, Bazilevs Y, Sacks MS, Hughes TJR. Fluid–structure interaction analysis of bioprosthetic heart valves: significance of arterial wall deformation. *Computational Mechanics* 2014; 54(4): 1055-1071. doi: 10.1007/s00466-014-1059-4

How to cite this article: R. Zorrilla, A. Larese and R. Rossi (2020), A discontinuous Nitsche-based Finite Element formulation for the imposition of the Navier-slip condition over embedded volumeless geometries, *Int J Numer Meth Fluids.*, *2020;00:0–0*.